

Entropy-based viscous regularization for the multi-dimensional Euler equations in low-Mach and transonic flows

Marc O. Delchini^a, Jean C. Ragusa^{*,a}, Ray A. Berry^b

^a*Department of Nuclear Engineering, Texas A&M University, College Station, TX 77843, USA*

^b*Idaho National Laboratory, Idaho Falls, ID 83415, USA*

Abstract

The entropy viscosity method, introduced by Guermond et al. [1, 2], is extended to the multi-dimensional Euler equations for both subsonic (very low Mach numbers) and supersonic flows. We show that the current definition of the viscosity coefficients [1, 2] is not adapted to low-Mach flows and we provide a robust alternate definition valid for any Mach number value. The new definitions are derived from a low-Mach asymptotic study. In addition, the entropy minimum principle is used to derive the viscous regularization terms for Euler equations with variable area for nozzle flow problems. Various 1-D and 2-D numerical tests are presented : flow in a convergent-divergent nozzle, Leblanc shock tube, slow moving shock, strong shock for liquid phase, subsonic flow around a 2-D cylinder and over a circular hump, and supersonic flow in a compression corner. Convergence studies are performed using analytical solutions in 1-D. The ideal gas and stiffened gas equations of state are employed.

Key words: entropy viscosity method, viscous stabilization method, low-Mach regime, shocks, Euler equations with variable area .

1. Introduction

not finished yet

Items to mention:

- low Mach solution techniques using compressible equations. need to recover the incompressible limit.
- entropy viscosity method, not yet assessed for low Mach and transonic flows

*Corresponding author

Email addresses: `delchmo@tamu.edu` (Marc O. Delchini), `jean.ragusa@tamu.edu` (Jean C. Ragusa), `ray.berry@inl.gov` (Ray A. Berry)

- 8 • low Mach also challenging when solved using compressible equations: if
- 9 explicit, time step $\rightarrow 0$. We use MOOSE and implicit time stepping
- 10 • some flow problems have both low Mach and supersonic regions
- 11 • OTHERS ???
- 12 •

13 Over the past years an increasing interest raised for computational meth-
 14 ods that can solve both compressible and incompressible flows. In engineering
 15 applications, there is often the need to solve for complex flows where a near
 16 incompressible regime or low Mach flow coexists with a supersonic flow domain.
 17 For example, such flow are encountered in aerodynamic in the study of airships.
 18 In the nuclear industry, flows are nearly the incompressible regime but com-
 19 pressible effects cannot be neglected because of the heat source and thus needs
 20 to be accurately resolved.

21 When solving the multi-D Euler equations for a wide range of Mach numbers,
 22 multiple problems have to address: stability, accuracy and acceleration of the
 23 convergence in the low Mach regime. Because of the hyperbolic nature of the
 24 equations, shocks can form during transonic and supersonic flows, and require
 25 the use of the numerical methods in order to stabilize the scheme and cor-
 26 rectly resolve the discontinuities. The literature offers a wide range of stabiliza-
 27 tion methods: flux-limiter [4, 5], pressure-based viscosity method ([6]), Lapidus
 28 method ([7, 8, 9]), and the entropy-viscosity method([1, 2]) among others. These
 29 numerical methods are usually developed using simple equation of states and
 30 tested for transonic and supersonic flows where the disparity between the acous-
 31 tic waves and the fluid speed is not large since the Mach number is of order one.
 32 This approach leads to a well-known accuracy problem in the low Mach regime
 33 where the fluid velocity is smaller that the speed of sound by multiple order of
 34 magnitude. The numerical dissipative terms become ill-scaled in the low Mach
 35 regime and lead to the wrong numerical solution by changing the nature of the
 36 equations solved. This behavior is well documented in the literature [10, 11, 12]
 37 and often treated by performing a low Mach asymptotic study of the multi-D
 38 Euler equation. This method was originally used [10] to show convergence of
 39 the compressible multi-D Euler equations to the incompressible ones. Thus,
 40 by using the same method, the effect of the dissipative terms in the low Mach
 41 regime, can be understood and, when needed, a fix is developed in order to
 42 ensure the convergence of the equations to the correct physical solution. This
 43 approach was used as a fixing method for multiple well known stabilization
 44 methods alike Roe scheme ([13]) and SUPG [12] while preserving the original
 45 stabilization properties of shocks.

46 We propose, through this paper, to investigate how the entropy viscosity method,
 47 when applied to the multi-D Euler equations with variable area, behaves in the
 48 low Mach regime. This method was initially introduced by Guermond et al.
 49 to solve for the hyperbolic systems and has shown good results when used for
 50 solving the multi-D Euler equations with various discretization schemes. More

51 importantly, it is simple to implement, can be used with unstructured grids,
 52 and its dissipative terms are consistent with the entropy minimum principle
 53 and proven valid for any equation of state under certain conditions [14].
 54

55 2. The Entropy Viscosity Method

56 2.1. Background

57 The Euler equations are given by

$$\partial_t \rho + \vec{\nabla} \cdot (\rho \vec{u}) = 0 \quad (1a)$$

$$\partial_t (\rho \vec{u}) + \vec{\nabla} \cdot (\rho \vec{u} \otimes \vec{u} + P \mathbb{I}) = 0 \quad (1b)$$

$$\partial_t (\rho E) + \vec{\nabla} \cdot [\vec{u} (\rho E + P)] = 0 \quad (1c)$$

60 where ρ , $\rho \vec{u}$ and ρE are the density, the momentum and the total energy, re-
 61 spectively, and will be referred to as the conservative variables. \vec{u} is the fluid
 62 velocity and its specific internal energy is denoted by $e = E - \frac{u^2}{2}$. An equation
 63 of state, dependent upon ρ and e , is used to compute the pressure P . The tensor
 64 product $\vec{a} \otimes \vec{b}$ is such that $(\vec{a} \otimes \vec{b})_{i,j} = a_i b_j$. The identity tensor is denoted by \mathbb{I} .

65 Next, the entropy viscosity method [1, 2, 16, 17] applied to Eq. (1) is recalled.
 66 The method consists of adding dissipative terms with a viscosity coefficient mod-
 67 ulated by the entropy production; this allows for a high-order accuracy when
 68 the solution is smooth (provided that the spatial and temporal discretizations
 69 also are high order). The derivation of the viscous regularization (or dissipative
 70 terms) is carried out to be consistent with the entropy minimum principle; de-
 71 tails and proofs of the derivation can be found in [14]. The viscous regularization
 72 thus obtained is valid for any equation of state as long as the physical entropy
 73 function s is such that $-s$ is a convex function with respect to the internal en-
 74 ergy e and the specific volume $1/\rho$. Euler equations with viscous regularization
 75 are given in Eq. (2):

$$\partial_t \rho + \vec{\nabla} \cdot (\rho \vec{u}) = \vec{\nabla} \cdot (\kappa \vec{\nabla} \rho) \quad (2a)$$

$$\partial_t (\rho \vec{u}) + \vec{\nabla} \cdot (\rho \vec{u} \otimes \vec{u} + P \mathbb{I}) = \vec{\nabla} \cdot (\mu \rho \vec{\nabla}^s \vec{u} + \kappa \vec{u} \otimes \vec{\nabla} \rho) \quad (2b)$$

$$\partial_t (\rho E) + \vec{\nabla} \cdot [\vec{u} (\rho E + P)] = \vec{\nabla} \cdot \left(\kappa \vec{\nabla} (\rho e) + \frac{1}{2} \|\vec{u}\|^2 \kappa \vec{\nabla} \rho + \rho \mu \vec{u} \vec{\nabla} \vec{u} \right) \quad (2c)$$

78 where κ and μ are positive viscosity coefficients. $\vec{\nabla}^s \vec{u}$ denotes the symmetric
 79 gradient operator that guarantees the method to be rotationally invariant [14].
 80 The viscosity coefficients are key ingredients in the viscous regularization of
 81 Eq. (2). Other stabilization approaches have been proposed in the literature,
 82 for instance, the Lapidus method [9, 7] or pressure-based viscosity methods
 83 [6]. Here, we follow the work of Guermond et al. and define the viscosity
 84 coefficients, κ and μ , based on the local entropy production. These coefficients
 85 are numerically evaluated using the local entropy residual $R_e(\vec{r}, t)$ defined in

Eq. (3); $R_e(\vec{r}, t)$ is known to be peaked in shocks and vanishingly small elsewhere [18].

$$R_e(\vec{r}, t) := \partial_t s + \vec{u} \cdot \vec{\nabla} s \quad (3)$$

In the current version of the method, the ratio of κ to μ is defined as a numerical Prandtl number, $Pr = \kappa/\mu$. Pr is a user-defined parameter and is usually taken in the range $[0.001; 1]$. Since the entropy residual $R_e(\vec{r}, t)$ may be extremely large in shocks, the definition of the viscosity coefficients also includes a first-order viscosity coefficient that serves as upper bound for the entropy-based viscosity coefficients. The first-order viscosity coefficients, denoted by μ_{\max} and κ_{\max} , are chosen so that the numerical scheme becomes equivalent to the upwind scheme when the first-order coefficients are employed. The upwind scheme is known to be over-dissipative but guarantees monotonicity [18]. In practice, the viscosity coefficients only saturate to the first-order viscosity coefficients in shocks and are much smaller elsewhere, hence avoiding over-dissipation due to the upwind method. The first-order viscosity coefficients μ_{\max} and κ_{\max} are equal and set proportional to the largest local eigenvalue $\|\vec{u}\| + c$:

$$\mu_{\max}(\vec{r}, t) = \kappa_{\max}(\vec{r}, t) = \frac{h}{2} (\|\vec{u}(t, \vec{r})\| + c(t, \vec{r})), \quad (4)$$

where h denotes the local grid size (for higher than linear finite element representations, h is defined as the ratio of the grid size to the polynomial order of the test functions used, see Eq. 2.4 in [17]). For simplicity, the first-order viscosity coefficient will only be referred to as the $\kappa_{\max}(\vec{r}, t)$. In practice, these quantities are evaluated within a given cell K at quadrature points:

$$\kappa_{\max}^K(\vec{r}_q, t) = \frac{h_K}{2} (\|\vec{u}(t, \vec{r}_q)\| + c(t, \vec{r}_q)), \quad (5)$$

where \vec{r}_q denotes the position of a quadrature point. As stated earlier, the entropy viscosity coefficients, which we denote by κ_e and μ_e , are set proportional to the entropy production evaluated by computing the local entropy residual R_e . The definitions also include the inter-element jump of the entropy flux $J[s]$, allowing for the detection of discontinuities other than shocks (e.g., contact).

$$\mu_e^K(\vec{r}_q, t) = h_K^2 \frac{\max(|R_e^K(\vec{r}_q, t)|, J^K[s](t))}{\|s - \bar{s}\|_\infty} \quad (6a)$$

$$\kappa_e^K(\vec{r}_q, t) = Pr \mu_e^K(\vec{r}_q, t) \quad (6b)$$

where $\|\cdot\|_\infty$ and $\bar{\cdot}$ denote the L_∞ -norm and the average operator over the entire computational domain, respectively. The definition of the entropy jump $J[s]$ is spatial discretization-dependent and examples of definitions can be found in [17] for discontinuous Galerkin discretization. For continuous finite element methods (FEM), the jump of a given quantity is defined as the inter-element change in its normal derivative ($\partial_n = \vec{\nabla} \cdot \vec{n}$) along the common face separating the two

elements. We take the largest value over all faces f present on the boundary ∂K of element K :

$$J^K[s](t) = \max_{f \in \partial K} \max_{\vec{r}_q \in f} [\vec{\nabla} s(\vec{r}_q, t) \cdot \vec{n}(\vec{r}_q)]_f, \quad (7)$$

where $[a(\vec{r}_q)]_f$ denotes the inter-element jump in $a(\vec{r})$ at quadrature point \vec{r}_q on face f . The denominator $\|s - \bar{s}\|_\infty$ is used for dimensionality purposes. Currently, there are no theoretical justification for choosing the denominator beyond a dimensionality argument. Finally, the viscosity coefficients μ and κ are as follows:

$$\mu(\vec{r}, t) = \min(\mu_e(\vec{r}, t), \mu_{\max}(\vec{r}, t)) \quad \text{and} \quad \kappa(\vec{r}, t) = \min(\kappa_e(\vec{r}, t), \kappa_{\max}(\vec{r}, t)). \quad (8)$$

Given these definitions, we have the following properties. In shock regions, the entropy viscosity coefficients will experience a peak because of entropy production and thus will saturate to the first-order viscosity. The first-order coefficients are known to be over-dissipative and will smooth out any oscillatory behavior. Elsewhere in the domain, entropy production will be small and the viscosity coefficients μ and κ will remain small. High-order accuracy for entropy-based viscous stabilization was demonstrated using several 1-D shock tube examples and various 2-D tests [1, 2, 17].

2.2. Issues in the Low-Mach Regime

In the low-Mach Regime, the flow is known to be isentropic, resulting in very little entropy production. Since the entropy viscosity method is directly based on the evaluation of the local entropy production, it is of interest to study how the entropy viscosity coefficients μ_e and κ_e scale in the low-Mach regime. In practice, the entropy residual R_e will be very small in that regime and so will be the denominator $\|s - \bar{s}\|_\infty$, thus making the definition of the viscosity coefficients in Eq. (6) undetermined and likely ill-scaled. One possible approach would consist of expanding the numerator and denominator in terms of the Mach number and deriving its limit when the Mach number goes to zero. Such derivation may not be straightforward, especially for general equations of state. However, this can be avoided by noting that the entropy residual R_e can be recast as a function of pressure, density, velocity, and speed of sound as shown in Eq. (9) of Section 3.1. This alternate entropy residual definition is the basis for the low-Mach analysis carried out in this paper and possesses several advantages that are detailed next.

3. An All-speed Reformulation of the Entropy Viscosity Method

In this section, the entropy residual R_e is recast as a function of pressure, density, velocity and speed of sound. Then, a low-Mach asymptotic study is carried out for the Euler equations with viscous regularization in order to derive an appropriate normalization parameter that is valid in the low-Mach regime as well as for transonic and supersonic flows.

3.1. New Definition of the Entropy Production Residual

The first step in defining viscosity coefficients that behave well in the low-Mach limit is to recast the entropy residual in terms of thermodynamic variables. This provides physical insight on possible normalization choices that can be valid in both low-Mach and transonic flows. The alternate definition of the entropy residual is given in Eq. (9). The derivation that leads to this equation is provided in Appendix A.

$$R_e(\vec{r}, t) := \partial_t s + \vec{u} \cdot \vec{\nabla} s = \frac{Ds}{Dt} = \frac{s_e}{P_e} \underbrace{\left(\frac{DP}{Dt} - c^2 \frac{D\rho}{Dt} \right)}_{\widetilde{R}_e(\vec{r}, t)}, \quad (9)$$

where $\frac{D}{Dt}$ denotes the material derivative ($\frac{D}{Dt} := \frac{\partial}{\partial t} + \vec{u} \cdot \vec{\nabla}$), and x_y is the standard shortcut notation for the partial derivative of x with respect to y , e.g., $P_e := \frac{\partial P}{\partial e}$. The entropy residuals R_e and \widetilde{R}_e are proportional to one another and will experience similar variations in space and time. Thus, one may elect to employ \widetilde{R}_e instead of R_e for the evaluation of the local entropy residual. The new expression presents several advantages:

- an analytical expression of the entropy function s is no longer needed: the residual \widetilde{R}_e is evaluated using the local values of pressure, density, velocity and speed of sound. Deriving an entropy function for some complex equation of states may be difficult;
- suitable normalizations for the residual \widetilde{R}_e can be devised. Examples include the pressure itself or combinations of the density, the speed of sound and the norm of the velocity, i.e., ρc^2 , $\rho c ||\vec{u}||$ or $\rho ||\vec{u}||^2$.

Denoting the normalization of \widetilde{R}_e by norm_P , the entropy-based viscosity coefficients μ_e and κ_e can be re-defined as follows:

$$\mu_e^K(\vec{r}, t) = h_K^2 \frac{\max \left(|\widetilde{R}_e^K(\vec{r}_q, t)|, ||\vec{u}(\vec{r}_q, t)|| J^K[P](t), ||\vec{u}(\vec{r}_q, t)|| c^2(\vec{r}_q, t) ||J^K[\rho](t)|| \right)}{\text{norm}_P^\mu}, \quad (10a)$$

and

$$\kappa_e^K(\vec{r}, t) = h_K^2 \frac{\max \left(|\widetilde{R}_e^K(\vec{r}_q, t)|, ||\vec{u}(\vec{r}_q, t)|| J^K[P](t), ||\vec{u}(\vec{r}_q, t)|| c^2(\vec{r}_q, t) ||J^K[\rho](t)|| \right)}{\text{norm}_P^\kappa}. \quad (10b)$$

Note that now the jump operator acts on the variables appearing in \widetilde{R}_e , namely, pressure and density. The μ and κ coefficients are kinematic viscosities (units of m^2/s); the normalization parameters norm_P are thus in units of pressure, hence the use of the subscript P . Note also that we are not requiring the same normalization for both μ_e and κ_e so the entropy viscosity coefficients can be different. The low-Mach asymptotic study presented next will determine the proper normalization.

3.2. Asymptotic Study in the Low-Mach Regime

The Euler equations with viscous stabilization, Eq. (6), bear some similarities with the Navier-Stokes equations in the sense that dissipative terms (containing second-order spatial derivatives) are present in both sets of equations. An abundant literature exists regarding the low-Mach asymptotics of the Navier-Stokes equations [10, 11, 12, 19]. The asymptotic study presented here is inspired by the work of Muller et al. [19] where an asymptotic derivation for the Navier-Stokes was presented. We remind the reader that the objective is to determine appropriate scaling for the entropy viscosity coefficients so that the dissipative terms remain well-scaled for two limit cases: (i) the isentropic limit where Euler equations degenerate to an incompressible system of equations in the low-Mach limit and (ii) the non-isentropic limit with formation of shocks. The isentropic limit of Euler equations with viscous regularization should yield the incompressible fluid flows results in the low-Mach limit, namely, that the pressure fluctuations are of the order M^2 and that the velocity satisfies the divergent constraint $\vec{\nabla} \cdot \vec{u}_0 = 0$ [10, 11, 12]. For non-isentropic situations, shocks may form for any value of Mach number and the minimum entropy principle should still be verified so that numerical oscillations, if any, be controlled by the entropy viscosity method independently of the value of the Mach number. Our objective is to determine the appropriate scaling for the Reynolds and Péclet numbers, Re_∞ and Pé_∞ , in these two limit cases.

In this Section, we are interested in the isentropic limit, the non-isentropic case is treated later. The first step in the study of the limit cases (i) and (ii) is to re-write Eq. (2) in a non-dimensional manner. In order to do so, the following variables are introduced:

$$\rho^* = \frac{\rho}{\rho_\infty}, \quad u^* = \frac{u}{u_\infty}, \quad P^* = \frac{P}{\rho_\infty c_\infty^2}, \quad E^* = \frac{E}{c_\infty^2},$$

$$x^* = \frac{x}{L_\infty}, \quad t^* = \frac{t}{L_\infty/u_\infty}, \quad \mu^* = \frac{\mu}{\mu_\infty}, \quad \kappa^* = \frac{\kappa}{\kappa_\infty}, \quad (11)$$

where the subscript ∞ denote the far-field or stagnation quantities and the superscript $*$ stands for the adimensional variables. The far-field reference quantities are chosen such that the dimensionless flow quantities are of order 1. The reference Mach number is given by

$$M_\infty = \frac{u_\infty}{c_\infty}, \quad (12)$$

where c_∞ is a reference value for the speed of sound. Then, the scaled Euler equations with viscous regularization are:

$$\partial_{t^*} \rho^* + \vec{\nabla}^* \cdot (\rho^* \vec{u}^*) = \frac{1}{\text{Pé}_\infty} \vec{\nabla}^* \cdot (\kappa^* \vec{\nabla}^* \rho^*) \quad (13a)$$

$$\partial_{t^*} (\rho^* \vec{u}^*) + \vec{\nabla}^* \cdot (\rho^* \vec{u}^* \otimes \vec{u}^*) + \frac{1}{M_\infty^2} \vec{\nabla}^* P^* = \frac{1}{\text{Re}_\infty} \vec{\nabla}^* \cdot (\rho^* \mu^* \vec{\nabla}^{s,*} \vec{u}^*)$$

$$+ \frac{1}{\text{Pé}_\infty} \vec{\nabla}^* \cdot (\vec{u}^* \otimes \kappa^* \vec{\nabla}^* \rho^*) \quad (13b)$$

$$\begin{aligned} \partial_{t^*}(\rho^* E^*) + \vec{\nabla}^* \cdot [\vec{u}^* (\rho^* E^* + P^*)] &= \frac{1}{\text{Pé}_\infty} \vec{\nabla}^* \cdot (\kappa^* \vec{\nabla}^* (\rho^* e^*)) \\ &+ \frac{M_\infty^2}{\text{Re}_\infty} \vec{\nabla}^* \cdot (\vec{u}^* \rho^* \mu^* \vec{\nabla}^{s,*} \vec{u}^*) + \frac{M_\infty^2}{2\text{Pé}_\infty} \vec{\nabla}^* \cdot (\kappa^* (u^*)^2 \vec{\nabla}^* \rho^*) , \end{aligned} \quad (13c)$$

where the numerical Reynolds (Re_∞) and Péclet (Pé_∞) numbers are defined as follows:

$$\text{Re}_\infty = \frac{u_\infty L_\infty}{\mu_\infty} \text{ and } \text{Pé}_\infty = \frac{u_\infty L_\infty}{\kappa_\infty} . \quad (14)$$

Note that the Prandtl number used in the original version of the entropy viscosity method is simply given by

$$\text{Pr}_\infty = \text{Pé}_\infty / \text{Re}_\infty . \quad (15)$$

For simplicity, we use here the ideal gas equation of state; its non-dimensionalized expression is given by

$$P^* = (\gamma - 1) \rho^* \left(E^* - \frac{1}{2} M_\infty^2 (u^*)^2 \right) = (\gamma - 1) \rho^* e^* . \quad (16)$$

The numerical Reynolds and Péclet numbers defined in Eq. (14) are related to the entropy viscosity coefficients μ_∞ and κ_∞ . Thus, once a scaling (in powers of M_∞) is obtained for Re_∞ and Pé_∞ , the corresponding normalization parameters norm_P^μ and norm_P^κ will automatically be set. For brevity, the superscripts $*$ are omitted in the remainder of this section.

In the low-Mach isentropic limit, shocks cannot form and the compressible Euler equations are known to converge to the incompressible equations when the Mach number tends to zero. When adding dissipative terms, as is the case with the entropy viscosity method, the main properties of the low-Mach asymptotic limit have to be preserved. We begin by expanding each variable in powers of the Mach number. As an example, the expansion for the pressure is given by:

$$P(\vec{r}, t) = P_0(\vec{r}, t) + P_1(\vec{r}, t) M_\infty + P_2(\vec{r}, t) M_\infty^2 + \dots \quad (17)$$

By studying the resulting momentum equations for various powers of M_∞ , we observe the following: the leading order and first-order pressure terms, P_0 and P_1 , are spatially constant if and only if $\text{Re}_\infty = \text{Pé}_\infty = 1$. In this case, we have, at order M_∞^{-2} :

$$\vec{\nabla} P_0 = 0 \quad (18a)$$

and, at order M_∞^{-1} ,

$$\vec{\nabla} P_1 = 0 . \quad (18b)$$

Using the scaling $\text{Re}_\infty = \text{Pé}_\infty = 1$, the leading-order expressions for the continuity, momentum, and energy equations are:

$$\partial_t \rho_0 + \vec{\nabla} \cdot (\rho \vec{u})_0 = \vec{\nabla} \cdot (\kappa \vec{\nabla} \rho)_0 \quad (19a)$$

236

$$\partial_t (\rho \vec{u})_0 + \vec{\nabla} \cdot (\rho \vec{u} \otimes \vec{u})_0 + \vec{\nabla} P_2 = \vec{\nabla} \cdot (\rho \mu \vec{\nabla}^s \vec{u} + \kappa \vec{u} \otimes \vec{\nabla} \rho)_0 \quad (19b)$$

$$\partial_t(\rho E)_0 + \vec{\nabla} \cdot [\vec{u}(\rho E + P)]_0 = \vec{\nabla} \cdot (\kappa \vec{\nabla}(\rho e))_0 \quad (19c)$$

where the notation $(fg)_0$ means that we only keep the 0th order terms in the product fg . The leading-order of the equation of state is given by

$$P_0 = (\gamma - 1)(\rho E)_0. \quad (20)$$

Using Eq. (20), the energy equation can be recast as a function of the leading-order pressure, P_0 , as follows:

$$\partial_t P_0 + \gamma \vec{\nabla} \cdot (\vec{u} P)_0 = \vec{\nabla} \cdot (\kappa \vec{\nabla}(P))_0 \quad (21)$$

From Eq. (18a), we infer that P_0 is spatially constant. Thus, Eq. (21) becomes

$$\frac{1}{\gamma P_0} \frac{dP_0}{dt} = -\vec{\nabla} \cdot \vec{u}_0 \quad (22)$$

and, at steady state, we have

$$\vec{\nabla} \cdot \vec{u}_0 = 0. \quad (23)$$

That is, the leading-order of velocity is divergence-free. The same reasoning can be applied to the leading-order of the continuity equation (Eq. (19a)) to show that the material derivative of the density is zero:

$$\frac{D\rho_0}{Dt} := \partial_t \rho_0 + \vec{u}_0 \cdot \vec{\nabla} \rho_0 = 0. \quad (24)$$

Therefore, we conclude that by setting the Reynolds and Péclet numbers to one, the incompressible fluid results are retrieved in the low-Mach limit when employing the compressible Euler equations with viscous regularization terms present. In addition, the scaling of the Prandtl number can also be obtained using Eq. (15), hence clarifying the use of the numerical Prandtl in the original entropy viscosity method [1].

3.3. Scaling of Re_∞ and $Pé_\infty$ for non-isentropic flows

Next, we consider the non-isentropic case. Recall that even subsonic flows can present shocks (for instance, a step initial condition in the pressure will trigger shock formation, independently of the Mach number). The non-dimensionalized form of the Euler equations given in Eq. (13) provides some insight on the dominant terms as a function of the Mach number. This is particular obvious in the momentum equation, Eq. (13b), where the gradient of pressure is scaled by $1/M_\infty^2$. In the non-isentropic case, we no longer have $\frac{\vec{\nabla} P}{M_2} = \vec{\nabla} P_2$ and this pressure gradient term may need to be stabilized by some dissipative terms of the same scaling so as to prevent spurious oscillations from forming. This leads to the following three possible requirements regarding the non-dimensionalized Reynolds and Péclet numbers for non-isentropic flows: (a) $Re_\infty = M_\infty^2$ and $Pé_\infty = 1$, (b) $Re_\infty = 1$ and $Pé_\infty = M_\infty^2$, or (c) $Re_\infty = Pé_\infty = M_\infty^2$. Any of these choices will also affect the stabilization of the continuity and energy

equations. For instance, using a Péclet number equal to M_∞^2 may effectively stabilize the continuity equation in the shock region but this may also add an excessive amount of dissipation for subsonic flows at the location of the contact wave. Such a behavior may not be suitable for accuracy purpose, making options (b) and (c) inappropriate. The same reasoning, left to the reader, can be carried out for the energy equation (Eq. (13c)) and results in the same conclusion. The remaining choice, option (a), has the proper scaling: in this case, only the dissipation terms involving $\tilde{\nabla}^{s,*} \tilde{u}^*$ scale as $1/M_\infty^2$ since $\text{Re}_\infty = M_\infty^2$, leaving unaffected the regularization of the continuity equation since $\text{Pé}_\infty = 1$.

3.4. New normalization for the entropy residual

The study of the above limit cases yields two different possible scalings for the Reynolds number: $\text{Re}_\infty = 1$ in the isentropic case and $\text{Re}_\infty = M_\infty^2$ for non-isentropic case, whereas the numerical Péclet number always scales as one. In order to have a stabilization method valid for a wide range of Mach numbers, including situations with shocks, these two scalings should be combined in a unique definition. The non-dimensionalized entropy residual, \tilde{R}_e^* , scales differently flow types (isentropic and non-isentropic) [20]. For isentropic flows, the non-dimensionalized entropy residual is known to scale as the Mach number. For non-isentropic flows, the non-dimensionalized entropy residual is large and presents a peak at the location of the shock. Thus, by inspecting the *local* variation of the non-dimensionalized entropy residual, an appropriate transition for the scaling of the Reynolds number can be obtained:

$$\text{Re}_\infty = \begin{cases} M^2 & \text{if } |\tilde{R}_e^*| \geq M \text{ (i.e., non-isentropic flow)} \\ 1 & \text{otherwise} \end{cases} . \quad (25)$$

Now that we have determined a scaling for Re_∞ and Pé_∞ , the normalization parameters norm_P^μ and norm_P^κ can be finalized. For brevity, only the steps leading to the derivation of norm_P^κ are provided; the algebra for norm_P^μ is similar. Using the definition of the viscosity coefficients given in Eq. (10) and the scaling of Eq. (11), it can be shown that:

$$\kappa_\infty = \frac{\rho_\infty c_\infty^2 u_\infty L_\infty}{\text{norm}_{P,\infty}^\kappa} , \quad (26)$$

where $\text{norm}_{P,\infty}$ is the reference far-field quantity for the normalization parameter norm_P . Substituting Eq. (26) into Eq. (14) and recalling that the numerical Péclet number scales as unity, we obtain:

$$\text{norm}_{P,\infty}^\kappa = \text{Pé}_\infty \rho_\infty c_\infty^2 = \rho_\infty c_\infty^2 . \quad (27)$$

Eq. (27) provides a proper normalization factor to define the κ viscosity coefficient. Similarly, the normalization parameter norm_P^μ for the μ viscosity coefficient is derived for the two cases given in Eq. (25):

$$\text{norm}_P^\mu = \text{Re}_\infty \rho_\infty c_\infty^2 = \begin{cases} \rho ||\tilde{u}||^2 & \text{if } |\tilde{R}_e^*| \geq M \text{ (i.e., non-isentropic flow)} \\ \rho c^2 = \text{norm}_P^\kappa & \text{otherwise} \end{cases} . \quad (28)$$

Finally, we summarize the definition of the viscosity coefficients μ and κ devised here:

$$\mu(\vec{r}, t) = \min \left(\mu_{\max}(\vec{r}, t), \mu_e(\vec{r}, t) \right) \text{ and } \kappa(\vec{r}, t) = \min \left(\mu_{\max}(\vec{r}, t), \kappa_e(\vec{r}, t) \right) \quad (29a)$$

where the first-order viscosity is given by

$$\kappa_{\max}(\vec{r}, t) = \mu_{\max}(\vec{r}, t) = \frac{h}{2} \left(\|\vec{u}\| + c \right) \quad (29b)$$

and the entropy viscosity coefficients by

$$\kappa_e(\vec{r}, t) = \frac{h^2 \max(\widetilde{R}_e, J)}{\rho c^2} \text{ and } \mu_e(\vec{r}, t) = \frac{h^2 \max(\widetilde{R}_e, J)}{\text{norm}_P^\mu} \quad (29c)$$

with the jumps given by

$$J = \|\vec{u}\| \max \left([[\vec{\nabla} P \cdot \vec{n}]], c^2 [[\vec{\nabla} \rho \cdot \vec{n}]] \right) \quad (29d)$$

where norm_P^κ is computed from Eq. (28). The jump J is a function of the jump of pressure and density gradients across the face with respect to its normal vector \vec{n} . Then, the largest value over all faces is determined and used in the definition of the viscosity coefficients.

With the definition of the viscosity coefficients μ and κ proposed in Eq. (29), the low-Mach asymptotic limit is ensured for isentropic flow and transonic flows with shocks will be correctly resolved. As the flow becomes locally supersonic, the viscosity coefficients μ and κ will be of the same order of magnitude which is consistent with the original definition of the entropy viscosity method [1, 2] recalled in Section 2.1.

4. Extension of the entropy viscosity technique Euler equations with variable area

Fluid flows in nozzles and in pipes of varying cross-sectional area can be modeled using the variable-area variant of the Euler equations, where the conservative variables are now multiplied by the area A . In addition, these equations differ from the standard Euler equations in that the momentum equation Eq. (30b) contains a non-conservative term proportional to the area gradient. For the purpose of this paper, the variable area is assumed to be a smooth function of space.

$$\partial_t (\rho A) + \vec{\nabla} \cdot (\rho \vec{u} A) = 0 \quad (30a)$$

$$\partial_t (\rho \vec{u} A) + \vec{\nabla} \cdot [A (\rho \vec{u} \otimes \vec{u} + P \mathbb{I})] = P \vec{\nabla} A \quad (30b)$$

$$\partial_t (\rho E A) + \vec{\nabla} \cdot [\vec{u} A (\rho E + P)] = 0 \quad (30c)$$

The application of the entropy viscosity method to the Euler equations with variable area is not fundamentally different to its application to the standard

328 Euler equations. However, we need to derive the associated dissipative terms
 329 and verify that the entropy minimum principle is still satisfied. The variable-
 330 area Euler equations with viscous regularization are given below; details of the
 331 derivation are provided in Appendix B.

$$\partial_t (\rho A) + \vec{\nabla} \cdot (\rho \vec{u} A) = \vec{\nabla} \cdot (A \kappa \vec{\nabla} \rho) \quad (31a)$$

$$\partial_t (\rho \vec{u} A) + \vec{\nabla} \cdot [A (\rho \vec{u} \otimes \vec{u} + P \mathbf{I})] = P \vec{\nabla} A + \vec{\nabla} \cdot [A (\mu \rho \vec{\nabla}^s \vec{u} + \kappa \vec{u} \otimes \vec{\nabla} \rho)] \quad (31b)$$

$$\partial_t (\rho A E) + \vec{\nabla} \cdot [\vec{u} A (\rho E + P)] = \vec{\nabla} \cdot \left[A \left(\kappa \vec{\nabla} (\rho e) + \frac{1}{2} \|\vec{u}\|^2 \kappa \vec{\nabla} \rho + \rho \mu \vec{u} \vec{\nabla}^s \vec{u} \right) \right] \quad (31c)$$

334 The dissipative terms are indeed very similar to the ones obtained for the stan-
 335 dard Euler equations: each dissipative flux is simply multiplied by the variable
 336 area A in order to ensure conservation of the dissipative flux. When assuming
 337 a constant area, Eq. (2) are recovered.

338 A low-Mach asymptotic limit of the multi-D Euler equations with variable
 339 area on the same model as in Section 3.2 will lead to the divergent constraint
 340 $\vec{\nabla} \cdot (\vec{u} A) = 0$ that can be recast as $\vec{\nabla} \cdot \vec{u} = -\vec{u} \cdot \vec{\nabla} A / A$. The gradient of the
 341 area acts as a source term and will force the fluid to accelerate or decelerate,
 342 depending on its sign.

343 5. Discretizations and Solution Techniques

344 In this section, we briefly describe the spatial and temporal techniques used
 345 to discretize and solve the system of equations Eq. (31). For conciseness, we
 346 re-write the system of equations in the following form:

$$\partial_t \mathbf{U} + \vec{\nabla} \cdot \vec{\mathbf{F}}(\mathbf{U}) = \mathbf{S} + \vec{\nabla} \cdot \mathbf{D}(\mathbf{U}) \vec{\nabla} \mathbf{U} \quad (32)$$

347 where $\mathbf{U} = [\rho A, \rho \vec{u} A, \rho E A]^T$ is the solution vector, \mathbf{F} denotes the inviscid flux

$$\vec{\mathbf{F}} \equiv \begin{bmatrix} \rho u A \\ (\rho u^2 + p) A \\ u(\rho E + P) A \end{bmatrix} \quad (33)$$

348 and \mathbf{S} is a source term that contains the non-conservative term $P \vec{\nabla} A$. The term
 349 $\vec{\nabla} \cdot \mathbf{D}(\mathbf{U}) \vec{\nabla} \mathbf{U}$ stands for the artificial dissipative terms.

350 5.1. Spatial and Temporal Discretizations

351 The system of equations given in Eq. (32) is discretized using a continuous
 352 Galerkin finite element method and temporal integrators available through the
 353 MOOSE multiphysics framework [21].

354 5.1.1. Continuous Finite Elements

In order to apply the continuous finite element method, Eq. (32) is multiplied by a test function $\mathbf{W}(\vec{r})$, integrated by parts and each integral is decomposed into a sum of integrals over each element K of the discrete mesh Ω . The following weak form is obtained:

$$\begin{aligned} \sum_K \int_K \partial_t \mathbf{U} \mathbf{W} - \sum_K \int_K \vec{\mathbf{F}}(\mathbf{U}) \cdot \vec{\nabla} \mathbf{W} + \int_{\partial\Omega} \vec{\mathbf{F}}(\mathbf{U}) \cdot \vec{n} \mathbf{W} - \sum_K \int_K \mathbf{S} \mathbf{W} \\ + \sum_K \int_K D(\mathbf{U}) \vec{\nabla} \mathbf{U} \cdot \vec{\nabla} \mathbf{W} - \int_{\partial\Omega} D(\mathbf{U}) \vec{\nabla} \mathbf{U} \cdot \vec{n} \mathbf{W} = 0 \end{aligned} \quad (34)$$

355 The integrals over the elements K are evaluated using a numerical quadrature.
 356 The MOOSE framework provides a wide range of test functions and quadrature
 357 rules. Linear Lagrange polynomials are employed as test functions in the re-
 358 sults section. Second-order spatial convergence will be demonstrated for smooth
 359 solutions.

360 5.1.2. Temporal integration

361 The MOOSE framework offers both first- and second-order explicit and im-
 362 plicit temporal integrators. In all of the numerical examples presented in Sec-
 363 tion 6, the temporal derivative will be evaluated using the second-order tempo-
 364 ral integrator BDF2. By considering three consecutive solutions, U^{n-1} , U^n and
 365 U^{n+1} , at times t^{n-1} , t^n and t^{n+1} , respectively, BDF2 can be expressed as:

$$\int_K \partial_t \mathbf{U} \mathbf{W} = \int_K (\omega_0 \mathbf{U}^{n+1} + \omega_1 \mathbf{U}^n + \omega_2 \mathbf{U}^{n-1}) \mathbf{W} \quad (35)$$

with

$$\begin{aligned} \omega_0 = \frac{2\Delta t^{n+1} + \Delta t^n}{\Delta t^{n+1} (\Delta t^{n+1} + \Delta t^n)}, \quad \omega_1 = -\frac{\Delta t^{n+1} + \Delta t^n}{\Delta t^{n+1} \Delta t^n} \\ , \text{ and } \omega_2 = \frac{\Delta t^{n+1}}{\Delta t^n (\Delta t^{n+1} + \Delta t^n)} \end{aligned}$$

366 where $\Delta t^n = t^n - t^{n-1}$ and $\Delta t^{n+1} = t^{n+1} - t^n$.

367 5.2. Boundary conditions

368 Boundary conditions are implemented by performing a characteristic decom-
 369 position to compute the appropriate flux at the boundaries. Our implementation
 370 of the subsonic boundary conditions is inspired of the method described in [22]
 371 and was adapted for an temporal implicit solver. Neumann boundary conditions
 372 are used for all of the boundary types, but for the inlet supersonic boundary
 373 that are imposed with Dirichlet boundary conditions.

374 For each numerical solution presented in Section 6, the type of boundary
 375 conditions used will be specified and taken ??? the followings: super-
 376 sonic inlet, subsonic inlet (stagnation pressure boundary) and supersonic outlet.

377 The artificial diffusion coefficient $D(\mathbf{U})$ is set to zero at the boundary of the
 378 computational domain so that the boundary term $\int_{\partial\Omega} D(\mathbf{U}) \vec{\nabla} \mathbf{U} \cdot \vec{n} \mathbf{W}$ stem-
 379 ming from the integration by parts of the artificial dissipative terms in Eq. (34)
 380 is ignored.

381 5.3. Solver

382 A Jacobian-free-Newton-Krylov (JFNK) method is used to solve for the so-
 383 lution at the end of each time step. An approximate Jacobian matrix of the
 384 discretized equations was derived and implemented. Obtaining the matrix en-
 385 tries requires that the partial derivatives of pressure with respect to the conser-
 386 vative variables be known (this is relatively simple for the Stiffened and Ideal
 387 Gas equations of state but may be more complex for general equations of state).
 388 The contributions of the artificial dissipative terms to the Jacobian matrix are
 389 approximated by lagging the viscosity coefficients (computing them with the
 390 previous solution). For instance, this is shown in Eq. (36) for the dissipative
 391 terms present in the continuity equation:

$$\frac{\partial}{\partial \mathbf{U}} \left(\kappa \vec{\nabla} \cdot \rho \vec{\nabla} W \right) \simeq \kappa \vec{\nabla} \cdot \frac{\partial \rho}{\partial \mathbf{U}} \vec{\nabla} W, \quad (36)$$

392 where \mathbf{U} denotes any of the conservative variables (in the above, we have ne-
 393 glected $\frac{\partial \kappa}{\partial \mathbf{U}}$) and W denotes the component of \mathbf{W} associated with the continuity
 394 equation.

395 6. Numerical Results

396 1-D and 2-D Numerical solutions for the Euler equations with viscous reg-
 397 ularization using the entropy viscosity method are presented here. Our results
 398 validate the chosen definitions for the viscosity coefficients in the low-Mach limit
 399 and verify that the new definitions resolve shocks appropriately.

400 The first set of 1-D simulations consist of liquid water and steam flowing in
 401 a convergent-divergent nozzle. This test is of interest for multiple reasons: (a)
 402 a steady state can be reached (some stabilization methods are known to have
 403 difficulties reaching a steady state, [4, 5]), (b) an analytical solution is available
 404 and a space-time convergence study can be performed, (c) it can be performed
 405 for liquid and gas phases, the gas phase simulation presents a shocks while the
 406 liquid-phase simulation has a significantly lower Mach number. Next, a 1-D
 407 shock tube test (in a straight pipe) taking from the Leblanc test-case suite [23]
 408 is performed. This test is known to be more challenging than Sod shock tubes
 409 and the fluid's Mach number varies spatially between 0 and 5. A convergence
 410 study is also performed in order to demonstrate convergence of the numerical
 411 solution to the exact solution. A slow moving shock is also investigated [24].
 412 This test helps in assessing the ability of the method at damping the post-
 413 shock low frequency noise. Finally, a strong shock for a liquid phase is also
 414 investigated. [need ref for this](#)

ρ_{left}	u_{left}	P_{left}	ρ_{right}	u_{right}	P_{right}
Leblanc shock tube (Section 6.3)					
1	0	$4 \cdot 10^{-2}$	10^{-3}	0	$4 \cdot 10^{-11}$
Strong shock for liquid phase (Section 6.4)					
1000	0	10^9	1000	0	10^5
Slow moving shock (Section 6.5)					
1	-0.81	1	3.86	-3.44	10.33

Table 1: Initial conditions for the 1-D shock tube tests.

415 The initial conditions (density in $kg.m^{-3}$, velocity in $m.s^{-1}$, pressure in Pa)
416 for the last three 1-D shock tubes are given in Table 1.

417 2-D simulations are presented next. First, subsonic flows of around a 2-D
418 cylinder [12] and over a Gaussian hump [25] are presented for various far-field
419 Mach numbers (as low of 10^{-7}). Numerical results of a transonic flow in a
420 compression corner are provided to illustrate the ability of the new viscosity
421 definitions to handle supersonic flows. Convergence studies are performed when
422 analytical solutions are available.

423 For each simulation, data relative to the boundary conditions, the Courant-
424 Friedrichs-Lewy number (CFL), mesh and equation of state are provided. All
425 of the numerical solution presented are obtained using BDF2 as temporal in-
426 tegrator and linear (1-D mesh), \mathbb{P}_1 (2-D triangular mesh), \mathbb{Q}_1 (2-D quadran-
427 gular mesh) finite elements. The integrals are numerically computed using a
428 second-order Gauss quadrature rule. The steady-state solution is detected by
429 monitoring the norm of the total residual (including all of the equations) and
430 reached when the norm of the total residual is below 10^{-6} . The ideal gas [26]
431 or stiffened gas equations of state [3] are used; a generic expression is given in
432 Eq. (37).

$$P = (\gamma - 1)\rho(e - q) - \gamma P_{\infty} \quad (37)$$

where the parameters q and P_{∞} are fluid-dependent and are given in Table 2.
The ideal gas equation of state is recovered by setting $q = P_{\infty} = 0$ in Eq. (37).
The entropy function for the stiffened gas equation of state is **convex** and given

Table 2: Stiffened Gas Equation of State parameters for steam and liquid water.

fluid	γ	$C_v (J.kg^{-1}.K^{-1})$	$P_{\infty} (Pa)$	$q (J.kg^{-1})$
liquid water (Section 6.1)	2.35	1816	10^9	$-1167 \cdot 10^3$
steam (Section 6.2)	1.43	1040	0	$2030 \cdot 10^3$
liquid water (Section 6.4)	4.4	1000	$6 \cdot 10^8$	0

by

$$s = C_v \ln \left(\frac{P + P_{\infty}}{\rho^{\gamma-1}} \right),$$

433 where C_v is the heat capacity at constant volume.

434

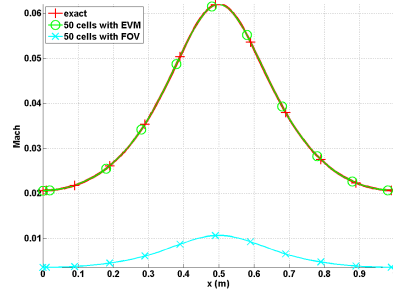
435 Finally, the convergence rates are computed using the following relation

$$rate_h = \ln \left(\frac{\|U_{2h} - U_{\text{exact}}\| - \|U_h - U_{\text{exact}}\|}{\|U_h - U_{\text{exact}}\|_h - \|U_{h/2} - U_{\text{exact}}\|} \right) / \ln 2 \quad (38)$$

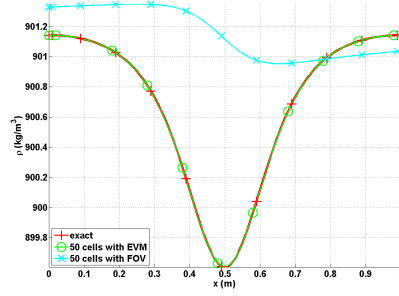
436 where $\|\cdot\|$ denotes either the L_1 or L_2 norms and h is the grid size.

437 6.1. Liquid water in a 1-D convergent-divergent nozzle

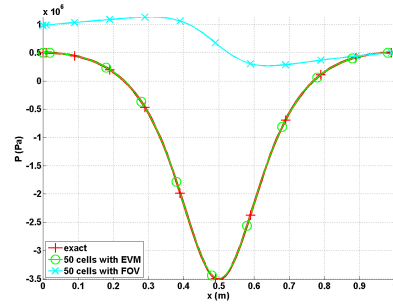
438 This simulation consists of liquid water flowing through a 1-D convergent-
439 divergent nozzle. The variable-area Euler equations are solved, with $A(x) =$
440 $1 + 0.5 \cos(2\pi x/L)$ where $L = 1m$ is the length of the nozzle. At the inlet, the
441 stagnation pressure and temperature are set to $P_0 = 1MPa$ and $T_0 = 453K$,
442 respectively. At the outlet, only the static pressure is specified: $P_s = 0.5MPa$.
443 Initially, the liquid is at rest, the temperature is uniform and equal to the
444 stagnation temperature and the pressure linearly decreases from the stagnation
445 pressure inlet value to the static pressure outlet value. The stiffened gas equa-
446 tion of state is used to model the liquid water with the parameters provided in
447 Table 2. Because of the low pressure difference between the inlet and the outlet,
448 the smooth initial conditions, and the large value of P_∞ , the flow remains sub-
449 sonic and thus does not display any shock. A detailed derivation of the exact
450 steady-state solution can be found in [27]. A uniform mesh of 50 cells was used
451 to obtain the numerical solution and the time step size was computed using a
452 CFL number of 750. Plots of the Mach number, density, and pressure are given
453 at steady-state in Fig. 1 for the numerical and exact solutions. The viscosity
454 coefficients are also graphed in Fig. 1d.



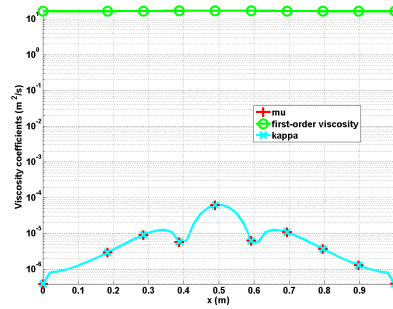
(a) Mach number



(b) Density



(c) Pressure



(d) Viscosity coefficients

Figure 1: Steady-state solution for a liquid flowing through a 1-D convergent-divergent nozzle.

455 In Fig. 1, the numerical solutions obtained using the first-order viscosity
456 (FOV) and the entropy viscosity method (EVM) are plotted against the exact
457 solution. The numerical solution obtained with the EVM and the exact solution
458 overlap, even for fairly coarse mesh (50 cells). On the other hand, the numerical
459 solution obtained with the FOV does not give the correct steady state: this is
460 an illustration of the effect of ill-scaled dissipative terms. Note that the entropy
461 viscosity coefficient is very small compared to the first-order one (Fig. 1d): (i)
462 the numerical solution is smooth as shown in Fig. 1 and (ii) the flow is in a
463 low-Mach regime and thus isentropic. A convergence study was performed
464 using the exact solution as a reference: the L_1 and L_2 norms of the error and
465 the corresponding convergence rates are computed at steady state on various
466 uniform mesh from 4 to 256 cells. Spatial convergence results using linear finite
467 elements are reported in Table 3 and Table 4 for the primitive variables: density,
468 velocity and pressure.

Table 3: L_1 norm of the error for the liquid phase in a 1-D convergent-divergent nozzle at steady state.

cells	density	rate	pressure	rate	velocity	rate
4	$2.8037 \cdot 10^{-1}$	—	$8.4705 \cdot 10^5$	—	7.2737	—
8	$1.3343 \cdot 10^{-1}$	0.495	$4.7893 \cdot 10^5$	0.24	6.1493	0.0747
16	$2.9373 \cdot 10^{-2}$	2.10	$1.0613 \cdot 10^5$	2.09	1.2275	2.25
32	$5.1120 \cdot 10^{-3}$	2.58	$1.8446 \cdot 10^4$	2.58	$1.8943 \cdot 10^{-1}$	2.78
64	$1.0558 \cdot 10^{-3}$	2.31	$3.7938 \cdot 10^3$	2.31	$3.7919 \cdot 10^{-2}$	2.37
128	$2.3712 \cdot 10^{-4}$	2.18	$8.4471 \cdot 10^2$	2.19	$8.5517 \cdot 10^{-3}$	2.17
256	$5.6058 \cdot 10^{-5}$	2.08	$1.9839 \cdot 10^2$	2.09	$2.0475 \cdot 10^{-3}$	2.07
512	$1.3278 \cdot 10^{-5}$	2.07	$4.6622 \cdot 10^1$	2.08	$4.9516 \cdot 10^{-4}$	2.06
1024	$3.1193 \cdot 10^{-6}$	—	$1.1755 \cdot 10^1$	—	$1.2379 \cdot 10^{-4}$	—

Table 4: L_2 norm of the error for the liquid phase in a 1-D convergent-divergent nozzle at steady state.

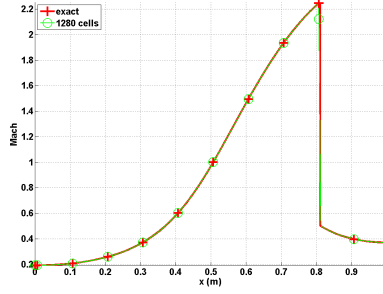
cells	density	rate	pressure	rate	velocity	rate
4	$3.106397 \cdot 10^{-1}$	—	$5.254445 \cdot 10^5$	—	3.288543	—
8	$7.491623 \cdot 10^{-2}$	2.06	$1.636966 \cdot 10^5$	1.62	1.823880	0.14
16	$2.079858 \cdot 10^{-2}$	1.81	$4.627338 \cdot 10^4$	1.77	$4.990605 \cdot 10^{-1}$	1.83
32	$5.329627 \cdot 10^{-3}$	1.96	$1.180287 \cdot 10^4$	1.96	$1.261018 \cdot 10^{-1}$	1.98
64	$1.341583 \cdot 10^{-3}$	1.99	$2.967104 \cdot 10^3$	1.99	$3.160914 \cdot 10^{-2}$	1.99
128	$3.359766 \cdot 10^{-4}$	1.99	$7.428087 \cdot 10^2$	1.99	$7.907499 \cdot 10^{-3}$	1.99
256	$8.403859 \cdot 10^{-5}$	1.99	$1.857861 \cdot 10^2$	2.01	$1.977292 \cdot 10^{-3}$	2.00
512	$2.10075 \cdot 10^{-5}$	—	$4.7024 \cdot 10^1$	—	$4.9516 \cdot 10^{-4}$	—

469 It is observed that the convergence rate for the L_1 and L_2 norm of the error

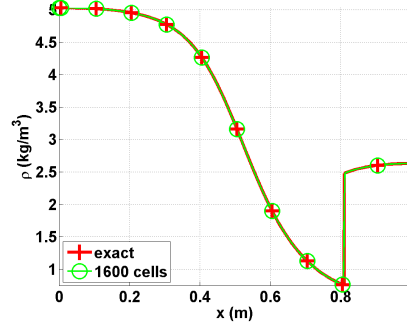
470 is 2: the entropy viscosity method preserves the high-order accuracy when the
 471 numerical solution is smooth, and the new definition of the entropy viscosity
 472 coefficient behaves appropriately in the low-Mach limit.

473 *6.2. Steam in a 1-D divergent-convergent nozzle*

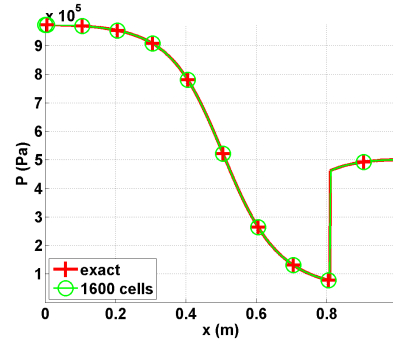
474 We use the same nozzle geometry, initial conditions and boundary conditions
 475 as in the previously example but replace liquid water with steam and use the
 476 steam parameters of the stiffened gas equation of state, Table 2. In this run,
 477 compressible effects will become dominant. The pressure difference between the
 478 inlet and outlet is large enough to accelerate the steam through the nozzle, lead-
 479 ing to a formation of shock in the divergent portion of the nozzle. The behavior
 480 is different from what was observed for the liquid water phase in Section 6.1
 481 because of the liquid to gas density ratio is about 1,000. An exact solution at
 482 steady state is available for the gas phase [27]. The aim of this section is to show
 483 that when using the new definitions of the viscosity coefficients (Eq. (29)), the
 484 shock can be correctly resolved without spurious oscillations. The steady-state
 485 numerical solution, obtained using a uniform mesh with 1600 cells, is shown in
 486 Fig. 2. The CFL was set to 80 (a high CFL value can be used since the shock
 487 is stationary).



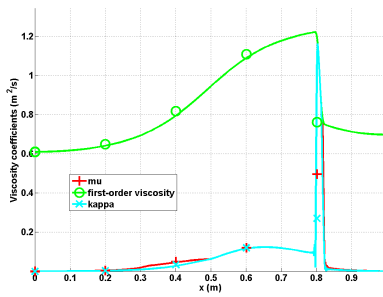
(a) Mach number



(b) Density



(c) Pressure



(d) Viscosity coefficients

20
Figure 2: Steady-state solution for vapor phase flowing in a 1-D convergent-divergent nozzle.

488 The steady-state solution of the density, Mach number and pressure are
 489 given in Fig. 2. The steady-solution exhibits a shock around $x = 0.8m$ and
 490 matches the exact solution. In Fig. 2d, the first-order and entropy viscosity
 491 coefficients are plotted at steady-state (on a log scale): the entropy viscosity
 492 coefficient is peaked in the shock region around $x = 0.8m$ as expected where it
 493 saturates to the first-order viscosity coefficient. The graph also presents another
 494 peak at $x = 0.5m$ corresponding to the position of the sonic point for a 1-D
 495 convergent-divergent nozzle. This particular point is known to develop small
 496 instabilities that are detected when computing the jumps of the pressure and
 497 density gradients. Anywhere else, the entropy viscosity coefficient is small. In
 498 order to prove convergence of the numerical solution to the exact solution, a
 499 convergence study is performed. Because of the presence of a shock, second-
 500 order accuracy is not expected and the convergence rate of a numerical solution
 501 should be 1 and $1/2$ when measured in the L_1 and L_2 norms, respectively (see
 502 Theorem 9.3 in [28]). Results are reported in Table 5 and Table 6 for the
 503 primitive variables: density, velocity and pressure. The convergence rates for
 504 the L_1 and L_2 norms of the error computed using Eq. (38) are in good agreement
 with the theoretical values.

Table 5: L_1 norm of the error for the vapor phase in a 1-D convergent-divergent nozzle at steady state.

cells	density	rate	pressure	rate	velocity	rate
5	$0.72562 \cdot 10^{-1}$	—	$1.5657 \cdot 10^5$	—	173.69	—
10	$0.4165 \cdot 10^{-1}$	0.80088	$9.6741 \cdot 10^4$	0.63425	120.69	0.52519
20	$0.20675 \cdot 10^{-1}$	1.0104	$4.9193 \cdot 10^4$	0.96971	72.149	0.74228
40	$0.093703 \cdot 10^{-1}$	1.1417	$2.0103 \cdot 10^4$	0.72728	34.716	1.0554
80	$0.047328 \cdot 10^{-1}$	0.9854	$1.0208 \cdot 10^4$	0.9777	16.082	1.1101
160	$0.023965 \cdot 10^{-2}$	0.9817	$5.1969 \cdot 10^3$	0.9739	7.9573	1.0150
320	$0.020768 \cdot 10^{-2}$	0.9886	$2.5116 \cdot 10^3$	1.0490	3.7812	1.0734
640	$0.0059715 \cdot 10^{-2}$	1.0160	$1.2754 \cdot 10^3$	0.9776	1.8353	1.0428

505

Table 6: L_2 norm of the error for the vapor phase in a 1-D convergent-divergent nozzle at steady state.

cells	density	rate	pressure	rate	velocity	rate
5	$9.7144 \cdot 10^{-1}$	—	$2.0215 \cdot 10^5$	—	236.94	—
10	$5.9718 \cdot 10^{-1}$	0.70195	$1.3024 \cdot 10^5$	0.63425	166.56	0.50854
20	$2.9503 \cdot 10^{-1}$	1.0173	$6.6503 \cdot 10^4$	0.96971	103.36	0.68831
40	$1.8193 \cdot 10^{-1}$	0.69747	$4.0171 \cdot 10^4$	0.72728	66.374	0.6390
80	$1.3366 \cdot 10^{-1}$	0.44485	$2.3163 \cdot 10^4$	0.43576	42.981	0.62692
160	$9.6638 \cdot 10^{-2}$	0.46790	$1.7263 \cdot 10^4$	0.42413	31.717	0.43844
320	$7.0896 \cdot 10^{-2}$	0.44688	$1.2763 \cdot 10^4$	0.43571	23.138	0.45499
640	$5.2191 \cdot 10^{-2}$	0.44190	$9.4217 \cdot 10^3$	0.43790	16.910	0.45238

6.3. Leblanc shock tube

The 1-D Leblanc shock tube is a Riemann problem designed to test the robustness and the accuracy of stabilization methods. The initial conditions are given in Table 1. The ideal gas equation of state (with $\gamma = 5/3$) is used to compute the pressure. This test is computationally challenging because of the large pressure ratio at the shock interface. The computational domain consists of a 1-D straight pipe of length $L = 9m$ with the initial interface located at $x = 2m$. At $t = 0.s$, the interface is removed. The numerical solution is run until $t = 4s$ and the density, momentum and total energy profiles are given in Fig. 3, along with the exact solution. The viscosity coefficients are also plotted in Fig. 3d. These plots were run with three different uniform mesh of 800, 3200 and 6000 cells and a constant $CFL = 1$.

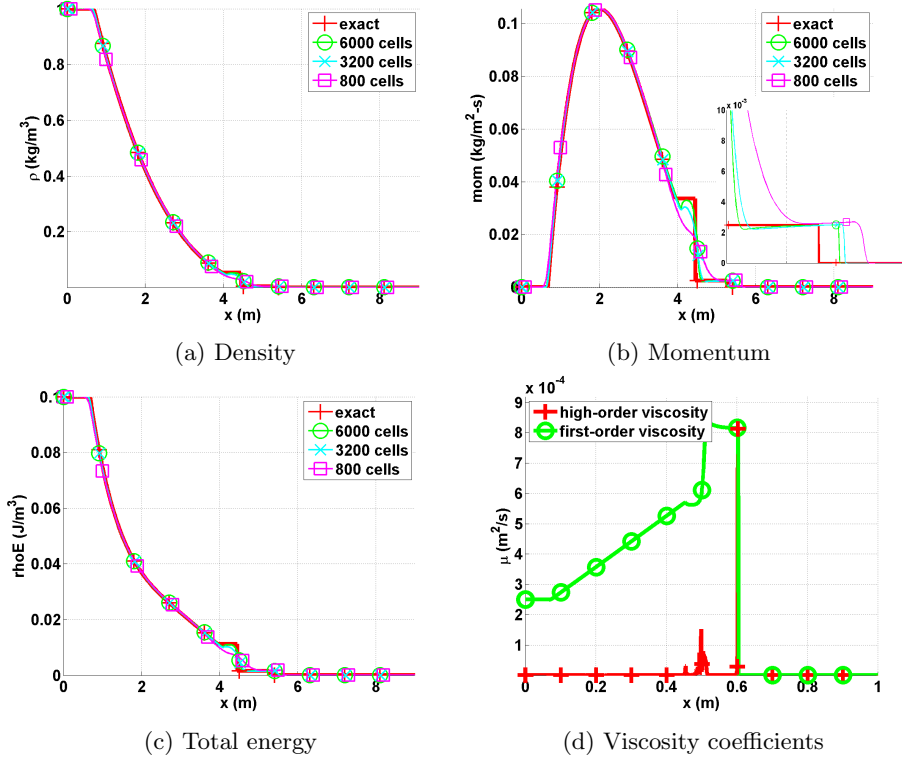


Figure 3: Exact and Numerical solutions for the 1-D Leblanc shock tube at $t = 4s$.

The density, momentum and total energy profiles are provided in Fig. 3. In Fig. 3b, the shock region is zoomed in for better resolution: the shock is well resolved. We also observe that the shock position computed numerically converges to the exact position under mesh refinement. The contact wave at $x = 4.5m$ can be seen in Fig. 3b. The entropy viscosity coefficient profile is shown in Fig. 3d and behaves as expected: it saturates to the first-order viscosity in the shock region, thus preventing oscillations from forming. At the location of the contact wave, a smaller peak is observed that is due to the presence of the jumps in the definition of the entropy viscosity coefficient (Eq. (29)). The Mach number, not plotted, is of the order of 1.3 right before the shock and reaches a maximum value close to 5 in the contact region.

Once again, a convergence study is performed in order to prove convergence of the numerical solution to the exact solution. As in the previous example (vapor phase in the 1-D nozzle, Section 6.2), the expected convergence rates in the L_1 and L_2 norms are 1 and $1/2$, respectively. The exact solution was obtained by running a 1-D Riemann solver and used as the reference solution to compute the L_1 and L_2 -norms that are reported in Table 7 and Table 8 for the

conservative variables: density, momentum and total energy. The convergence rates are again approaching the theoretical values.

Table 7: L_1 norm of the error for the 1-D Leblanc test at $t = 4s$.

cells	density	rate	momentum	rate	total energy	rate
100	$1.0354722 \cdot 10^{-2}$	—	$3.5471714 \cdot 10^{-3}$	—	$1.4033046 \cdot 10^{-3}$	—
200	$7.2680512 \cdot 10^{-3}$	0.51064841	$2.5933119 \cdot 10^{-3}$	0.45187331	$9.8611746 \cdot 10^{-4}$	0.5089968
400	$5.0825628 \cdot 10^{-3}$	0.51601245	$2.0668092 \cdot 10^{-3}$	0.32739054	$7.7844421 \cdot 10^{-4}$	0.34116585
800	$3.4025056 \cdot 10^{-3}$	0.57895861	$1.4793838 \cdot 10^{-3}$	0.48240884	$5.5702549 \cdot 10^{-4}$	0.48285029
1600	$2.1649953 \cdot 10^{-3}$	0.65223363	$9.7152832 \cdot 10^{-4}$	0.6066684	$3.5720171 \cdot 10^{-4}$	0.64100438
3200	$1.2465433 \cdot 10^{-3}$	0.79643094	$5.5937409 \cdot 10^{-4}$	0.79644263	$2.0491799 \cdot 10^{-4}$	0.80169235
6400	$6.4476928 \cdot 10^{-4}$	0.95107804	$3.0244198 \cdot 10^{-4}$	0.88715502	$1.0914891 \cdot 10^{-4}$	0.90874889
12800	$3.3950948 \cdot 10^{-4}$	0.92533116	$1.5958118 \cdot 10^{-4}$	0.9223679	$5.7909794 \cdot 10^{-5}$	0.91441847

Table 8: L_2 norm of the error for the 1-D Leblanc test at $t = 4s$.

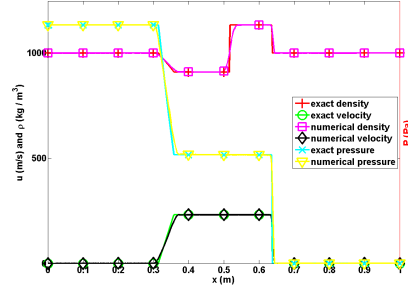
cells	density	rate	momentum	rate	total energy	rate
100	$5.7187851 \cdot 10^{-3}$	—	$1.7767236 \cdot 10^{-3}$	—	$7.6112265 \cdot 10^{-4}$	—
200	$3.8995238 \cdot 10^{-3}$	0.55241073	$1.4913161 \cdot 10^{-3}$	0.25263314	$5.5497308 \cdot 10^{-4}$	0.45571115
400	$2.8103526 \cdot 10^{-3}$	0.4725468	$1.3305301 \cdot 10^{-3}$	0.164585	$4.6063172 \cdot 10^{-4}$	0.26880405
800	$2.1081933 \cdot 10^{-3}$	0.41474398	$1.1398931 \cdot 10^{-3}$	0.22310254	$3.7798953 \cdot 10^{-4}$	0.28526749
1600	$1.5731052 \cdot 10^{-3}$	0.42239201	$9.0394227 \cdot 10^{-4}$	0.33459602	$2.9584646 \cdot 10^{-4}$	0.35349763
3200	$1.0610667 \cdot 10^{-3}$	0.56809979	$6.2735595 \cdot 10^{-4}$	0.52694639	$2.054455 \cdot 10^{-4}$	0.52609289
6400	$7.3309974 \cdot 10^{-4}$	0.53343397	$4.4545754 \cdot 10^{-4}$	0.49399631	$1.4670834 \cdot 10^{-4}$	0.48580482
12800	$5.1020991 \cdot 10^{-4}$	0.52291857	$3.1266758 \cdot 10^{-4}$	0.5106583	$1.0299897 \cdot 10^{-5}$	0.51032105

6.4. 1-D shock tube with a liquid phase

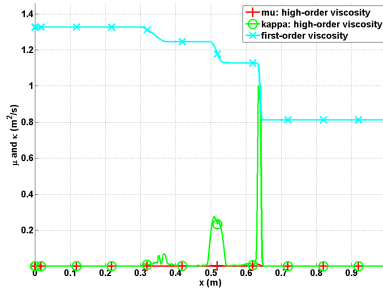
The purpose of this test is to investigate the ability of the entropy viscosity method to stabilize a strong shock with a small Mach number [29]: the Mach number in the shock region is of the order of 0.1. In this case, as explained in Section 3.2, the viscosity coefficients are required to have different order of magnitude in order to ensure the correct scaling of the dissipative terms. This test will allow us to validate the approach presented in Section 3.2.

The stiffened gas equation of state is used to model a liquid flow with the parameters given in Table 2. The computational domain of length $L = 1m$ is uniformly discretized using 500 cells. The step initial conditions are given in Table 1. The simulation is run with a $CFL = 1$ until the final time $t_{\text{final}} = 7 \cdot 10^{-5}s$. Results for pressure, density, velocity and the viscosity coefficients are given in Fig. 4 along with the exact solution for comparison purposes. The numerical solution is in good agreement with exact solution in Fig. 4a. The

viscosity coefficients μ and κ are not equal in the shock because the Mach number is of order 0.1. The viscosity coefficient κ saturates to the first-order viscosity in the shock region around $x = 0.65m$ and is sufficient to stabilize the numerical scheme.



(a) Density, velocity and pressure profiles.



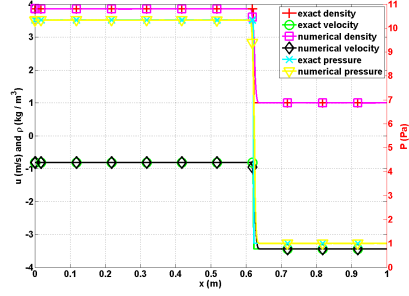
(b) Viscosity coefficients profile.

Figure 4: Numerical solution for the 1-D liquid shock tube at $t_{\text{final}} = 7 \cdot 10^{-5} s$.

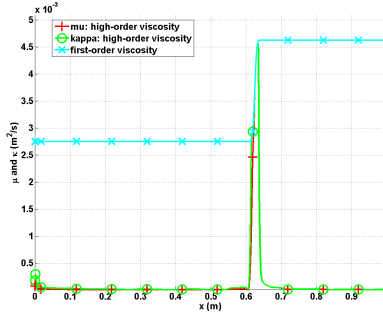
6.5. 1-D slow moving shock

Slow moving shocks are known to produce post-shock noise of low frequency that are not damped by some numerical dissipation methods [24]. The aim of this simulation is to test the ability of the entropy viscosity method to dampen the low frequency waves. The 1-D slow moving shock consists of a shock wave moving from left to right with the initial conditions given in Table 1. The ideal gas equation of state is used with a heat capacity ratio $\gamma = 1.4$. In order to make the shock travel a significant distance, the final time is taken equal to $t = 1.1s$. A pressure boundary condition is used at the left boundary to let the rarefaction and contact waves exit the domain. The numerical solution, obtained with 200 equally-spaced cells, is given in Fig. 5 and is compared to the exact solution obtained from a Riemann solver. We use a CFL of 1. With this CFL value, it takes about 50 time steps for the shock to traverse one cell. The numerical results are in good agreement with the exact solution and do not display any post-shock noise. The rarefaction and contact waves are not visible on Fig. 5a

570 since they exited the computational domain through the left pressure boundary
 571 condition earlier. As explained in [30], Godunov's type method usually fails to
 572 resolve a slow moving shock because of the nature of the stabilization method:
 573 the method scales as the eigenvalue of the appropriate field. In the case of a slow
 574 moving shock, the dissipation added to the system is under-estimated and leads
 575 to post-shock noise. In the case of the entropy viscosity method, the entropy
 576 residual detects the shock position and the viscosity coefficients saturate to the
 577 first-order viscosity values in the shock region. The main difference between a
 578 Godunov's type method and the entropy viscosity method relies in the definition
 579 of the first-order viscosity coefficients that are proportional to the *local maximum*
 580 *eigenvalue* $||\vec{u}|| + c$ and not to the eigenvalue of the characteristic field.



(a) Velocity, density and pressure



(b) Viscosity coefficients

Figure 5: Slow moving shock profiles at $t = 1.1s$.

581 6.6. Subsonic flow over a 2-D cylinder

582 Fluid flow over a 2-D cylinder is often used as a benchmark case to test nu-
 583 merical schemes in the low-Mach regime [10, 11, 12]. For this test, an analytical
 584 solution is available in the incompressible limit or low-Mach limit and is often
 585 referred to as the potential flow solution. The main features of the potential
 586 flow are the following:

- The solution is symmetric: the iso-Mach contour lines are used to assess the symmetry of the numerical solution;
- The velocity at the top of the cylinder is twice the incoming velocity set at the inlet;
- The pressure fluctuations are proportional to the square of inlet Mach number, i.e.,

$$\delta P = \frac{\max(P(\vec{r})) - \min(P(\vec{r}))}{\max(P(\vec{r}))} \propto M_\infty^2 \quad (39)$$

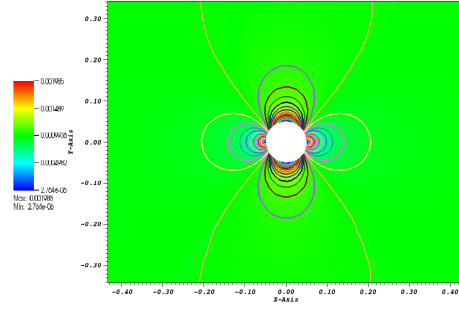
where δP and M_∞ denote the pressure fluctuations and the inlet Mach number, respectively.

The computational domain consists of a 1×1 square with a circular hole of radius 0.05 in its center. A \mathbb{P}_1 triangular mesh with 4008 triangular elements was used to discretize the geometry. The ideal gas equation of state, with $\gamma = 1.4$ is used. At the inlet, a subsonic stagnation boundary condition is used: the stagnation pressure and temperature are computed using the following relations:

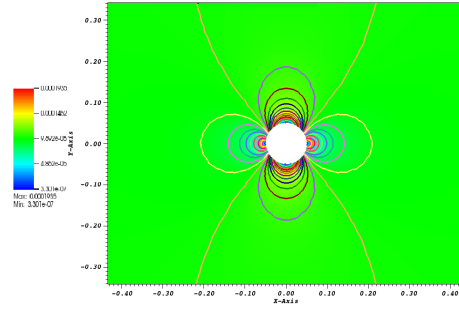
$$\begin{cases} P_0 = P \left(1 + \frac{\gamma-1}{2} M^2\right)^{\frac{\gamma}{\gamma-1}} \\ T_0 = T \left(1 + \frac{\gamma-1}{2} M^2\right) \end{cases} \quad (40)$$

An static pressure boundary condition is used for the outlet boundary and the following static pressure $P_s = 101,325 \text{ Pa}$ is set. The implementation of the pressure boundary conditions is based of [22]. A solid wall boundary condition is set for the top and bottom walls of the computational domain. The simulations are run until a steady state is reached with a CFL of 40. The steady state is considered reached when the residual norm (for all equations) is less than 10^{-12} .

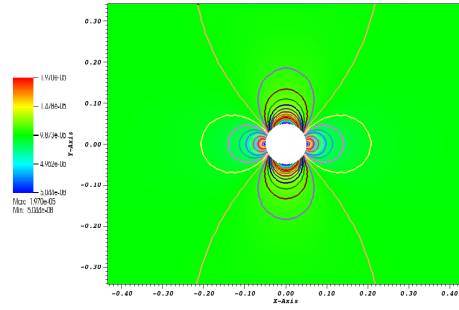
Several simulations are performed, with inlet Mach numbers M_{inlet} ranging from 10^{-3} to 10^{-7} , and are shown in Fig. 6. The iso-Mach contour lines are drawn using 30 equally-spaced intervals $2 \cdot 10^{-10}$ to M_{inlet} and allow us to assess the symmetry of the numerical solution.



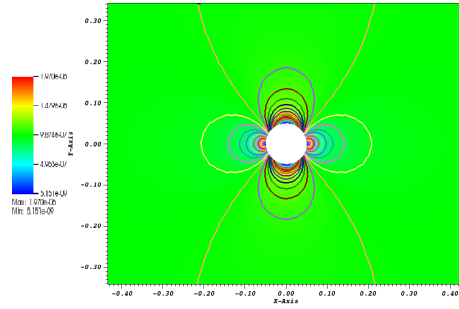
(a) $M_{\text{inlet}} = 10^{-3}$



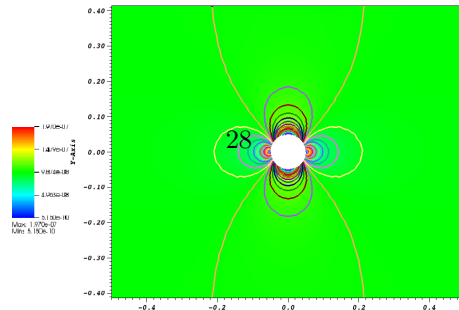
(b) $M_{\text{inlet}} = 10^{-4}$



(c) $M_{\text{inlet}} = 10^{-5}$



(d) $M_{\text{inlet}} = 10^{-6}$



(e) $M_{\text{inlet}} = 10^{-7}$

610 The velocity at the top of the cylinder and at the inlet are given for different
611 Mach-number values (ranging from 10^{-3} to 10^{-7}) in Table 9. The ratio of the
612 inlet velocity to the velocity at the top of cylinder is also computed and is very
613 close to the theoretical value of 2 that is expected in the incompressible limit.

Table 9: Velocity ratio for different Mach numbers.

Mach number	inlet velocity	velocity at the top of the cylinder	ratio
10^{-3}	$2.348 \cdot 10^{-3}$	$1.176 \cdot 10^{-3}$	1.99
10^{-4}	$2.285 \cdot 10^{-4}$	$1.145 \cdot 10^{-4}$	1.99
10^{-5}	$2.283 \cdot 10^{-5}$	$1.144 \cdot 10^{-5}$	1.99
10^{-6}	$2.283 \cdot 10^{-6}$	$1.144 \cdot 10^{-6}$	1.99
10^{-7}	$2.283 \cdot 10^{-7}$	$1.144 \cdot 10^{-7}$	1.99

614 In Fig. 7, the fluctuations in pressure and velocity are plotted as a function of
615 the Mach number (on a log-log scale). The fluctuations are expected to be of the
616 order of M^2 and M for the pressure and velocity, respectively. It is known that
617 some stabilization methods, e.g., [10, 11, 12], can produce pressure fluctuations
618 with the wrong Mach-number order. Here, entropy viscosity method yields the
619 correct order in the low-Mach limit. For ease of comparison, the reference lines
620 with slope values of 1 and 2 are also plotted.

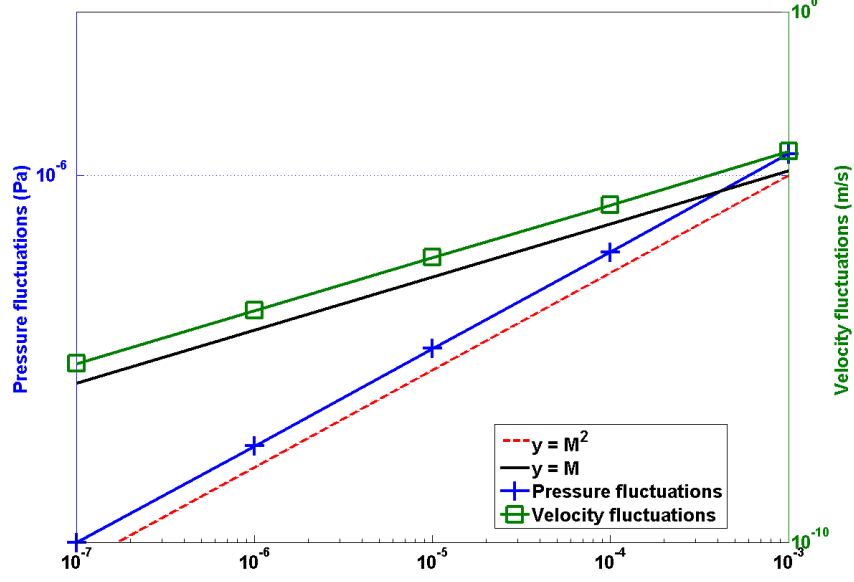


Figure 7: Log-log plot of the pressure and velocity fluctuations as a function of the far-field Mach number.

6.7. Subsonic flow over a 2-D hump

This is another example of an internal flow configuration. It consists of a channel of height $L = 1\text{ m}$ and length $3L$, with a circular bump of length L and thickness $0.1L$. The bump is located on the bottom wall at a distance L from the inlet. The system is initialized with a uniform pressure $P = 101,325\text{ Pa}$ and temperature $T = 300\text{ K}$. The initial velocity is computed from the inlet Mach number, the pressure, the temperature and the ideal gas equation (with $\gamma = 1.4$). Here, $C_v = 717\text{ J/kg} \cdot \text{K}$. At the inlet, a subsonic stagnation boundary condition is used and the stagnation pressure and temperature are computed using Eq. (40). The static pressure $P_s = 101,325\text{ Pa}$ is set at the subsonic outlet. The results are shown in Fig. 8a, Fig. 8b, Fig. 8c and Fig. 8d for inlet Mach numbers $M_\infty = 0.7$, $M_\infty = 0.01$, $M_\infty = 10^{-4}$ and $M_\infty = 10^{-7}$, respectively. It is expected that, within the low-Mach number range, the solution does not depend on the Mach number and is identical to the solution obtained with an incompressible flow code. On the other hand, for a flow at $M = 0.7$, the compressible effects become more important and shock can form. A uniform grid of 3352 Q_1 elements was used to obtain the numerical solution for Mach numbers below $M_\infty = 0.01$. A once-refined mesh was employed for the $M_\infty = 0.7$ simulation in order to better resolve the shock. A CFL of 20 was employed and the simulations were run until steady state.

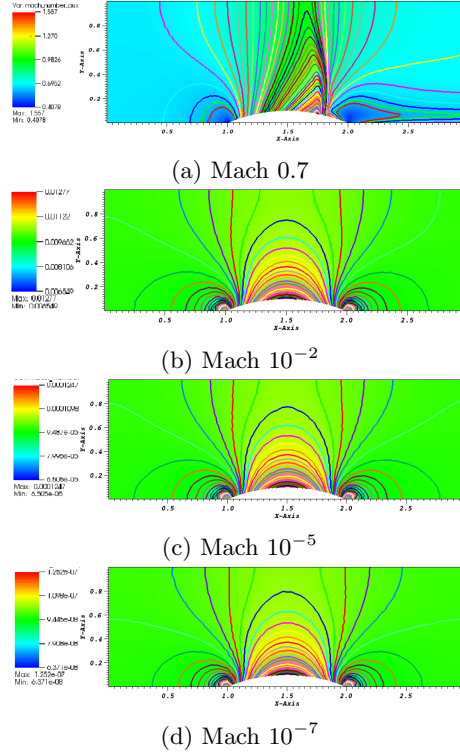


Figure 8: Iso-Mach lines for a 2-D flow over a circular bump (steady-state solution).

The results showed in Fig. 8b, Fig. 8c and Fig. 8d correspond to the low-Mach regime. The iso-Mach lines are drawn ranging from the minimum and the maximum values (provided in each legend) using 50 equally-spaced intervals. The steady-state solution is symmetric and does not depend on the value of the inlet Mach number, as expected in the incompressible limit.

In Fig. 8a, the steady-state numerical solution develops a shock: the compressibility effect are no longer negligible. The iso-Mach lines are also plotted with 50 intervals and range from 0.4 to 1.6. The shock is well resolved and does not display any instabilities or spurious oscillations. The results presented in Fig. 8 were obtained with the new definitions of the viscosity coefficients and illustrate the ability of the entropy viscosity method to correctly simulate several types of flows (subsonic and transonic flows) without tuning parameters.

6.8. Supersonic flow in a compression corner

In this last example, we consider a supersonic flow at Mach 2.5 impinging on a corner with an angle of 15° . From the oblique shock theory [15], an analytical solution for this supersonic flow is available and give the downstream

658 to upstream pressure, entropy and Mach number ratios. The initial conditions
659 are chosen to be spatially uniform: the pressure and temperature are set to $P =$
660 $101,325 \text{ Pa}$ and $T = 300 \text{ K}$, respectively. The ideal gas equation of state is used
661 with the same parameters as in Section 6.7. The initial velocity is computed from
662 the upstream Mach number. The inlet is supersonic and therefore, the pressure,
663 temperature and velocity are specified using Dirichlet boundary conditions. The
664 outlet is also supersonic and none of the characteristics enter the domain through
665 this boundary: the values will be computed by the implicit solver.

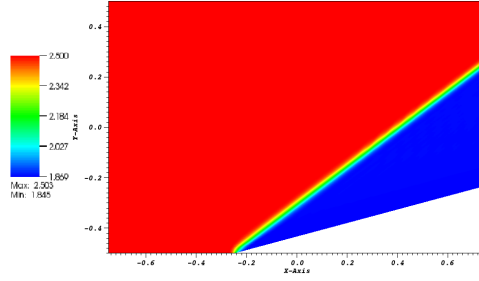
666 The simulation is run with $CFL = 2$, until steady state is reached. A 2-D
667 mesh made of 16,109 \mathbb{Q}_1 elements is used. The ratios for pressure, entropy and
668 Mach number computed using the analytical (published with only two significant
669 digits) and the numerical solutions are given in Table 10; they are in excellent
670 agreement. The shock wave angle at steady state is also known and given by
671 the so-called $\theta - \beta - M$ relation:

$$\tan \theta = 2 \cot \beta \frac{M^2 \sin^2 \beta - 1}{M^2 (\gamma + \cos^2(2\beta)) + 2}, \quad (41)$$

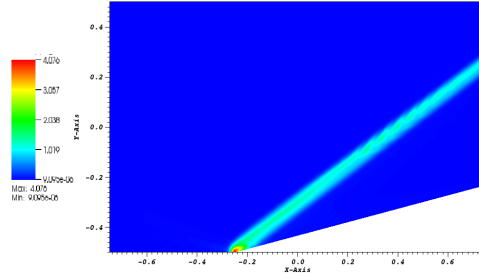
672 where θ , β and M denote the corner angle, the shock wave angle, and the
673 upstream Mach number, respectively. For Mach 2.5 and a 15° corner angle, the
674 analytical value for the shock wave angle is 36.94° at steady state. From Fig. 9a,
675 the numerical value of the shock wave angle can be measured and is found to
676 be equal to 36.9° , and thus in excellent agreement with theory.

	analytical	numerical
Pressure	2.47	2.467
Mach number	0.74	0.741
Entropy	1.03	1.026

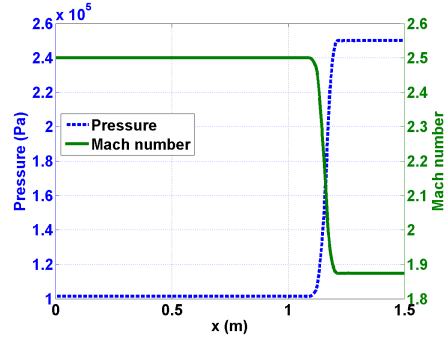
Table 10: Ratio of analytical and numerical downstream to upstream quantities for the compression corner problems (corner angle of 15° and inlet $M = 2.5$ (analytical values from [15])).



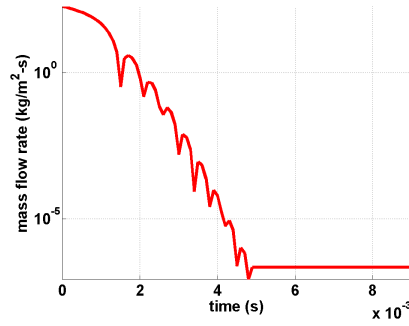
(a) Mach number



(b) Viscosity coefficients



(c) Pressure and Mach number



(d) Difference between inlet and outlet mass flow rates as a function of time.

Figure 9: Steady-state solution for a flow in a 2-D compression corner.

677 The steady-state numerical solution is given in Fig. 9: the Mach number and
 678 the viscosity coefficients are plotted in Fig. 9a and Fig. 9b, respectively. The
 679 steady-state solution is formed of two regions of constant states, separated by the
 680 oblique shock. Fig. 9b shows that the viscosity coefficient is large in the shock
 681 and small elsewhere, as expected. At the location of the corner ($x = -0.25m$,
 682 $y = -0.5m$), the viscosity coefficient is peaked because of the treatment of the
 683 wall boundary condition: at this particular node, the normal is not well defined
 684 and may cause some numerical errors. The 1-D graphs at $y = 0$ for the pressure
 685 and the Mach number are given in Fig. 9c: no spurious oscillations are observed
 686 and the shock is well resolved. Finally, the difference between the inlet and
 687 outlet mass flow rates is plotted in Fig. 9d which shows that a steady state has
 688 been reached.

689 7. Conclusions

690 A new version of the entropy viscosity method valid for a wide range of
 691 Mach number and applied to the multi-D Euler equations with variable area
 692 was derived and presented. The definition of the viscosity coefficient is now
 693 consistent with the low Mach asymptotic limit, does not require an analytical
 694 expression of the entropy function, and thus, could be used with any equation
 695 of state having a convex entropy. Tests were performed with the Ideal and
 696 Stiffened Gas equation of states. In 1-D, convergence of the numerical solu-
 697 tion (either smooth or with shocks) to the exact solution was demonstrated by
 698 computing the convergence rates of the L1 and L2 norms of the error for flows
 699 in convergence-divergent nozzle and a straight pipe. 2-D simulations were also
 700 performed for both subsonic and supersonic flows, and various geometries: the
 701 entropy viscosity method behaves well for a wide range of Mach number. The
 702 numerical results obtained for a flow over a circular bump (subsonic and tran-
 703 sonic flows) illustrates the capabilities of the method to adapt to the flow type.
 704 As future work, the entropy viscosity method will be extended to the 1-D seven
 705 equations model [22]. This two-phase flow system of equations is a good can-
 706 didate for two reasons: it is unconditionally hyperbolic and degenerates to the
 707 multi-D Euler equations when one phase disappears.

708 Acknowledgments

709 The authors (M.D. and J.R.) would like to thank Bojan Popov and Jean-Luc
 710 Guermond for many fruitful discussions.

711 References

- 712 [1] J. L. Guermond, R. Pasquetti, Entropy viscosity method for nonlinear con-
 713 servation laws, *Journal of Comput. Phys* 230 (2011) 4248–4267.

- 714 [2] J. L. Guermond, R. Pasquetti, Entropy viscosity method for high-order ap-
715 proximations of conservation laws, *Lecture Notes in Computational Science*
716 *and Engineering* 76 (2011) 411–418.
- 717 [3] O. LeMetayer, J. Massoni, R. Saurel, Elaborating equation of state for a
718 liquid and its vapor for two-phase flow models, *International Journal of*
719 *Thermal Science* 43 (2004) 265–276.
- 720 [4] B. Cockburn, C. Johnson, C. Shu, E. Tadmor, Advanced numerical approx-
721 imation of nonlinear hyperbolic equations, *Lecture Notes in Mathematics*
722 1697.
- 723 [5] B. Cockburn, G. Karniadakis, C. Shu, Discontinuous galerkin methods:
724 theory, computation and applications, *Lecture Notes in Computer Science*
725 *and Engineering* 11.
- 726 [6] R. Lohner, *Applied CFD Techniques: an Introduction based on Finite*
727 *Element Methods*, 2nd Edition Wiley, 2003.
- 728 [7] A. Lapidus, A detached shock calculation by second order finite differences,
729 *J. Comput. Phys.* 2 (1967) 154–177.
- 730 [8] R. Lohner, K. Morgan, J. Peraire, A simple extension to multidimensional
731 problems of the artificial viscosity due to lapidus, *Commun. Numer. Meth-*
732 *ods Eng.* 1(14) (1985) 141–147.
- 733 [9] J. Donea, A. Huerta, *Finite Element Methods for Flow Problems*, Oxford
734 University Press, 2003.
- 735 [10] H. Guillard, C. Viozat, On the behavior of upwind schemes in the low mach
736 number limit, *Computers & Fluids* 28 (1999) 63–86.
- 737 [11] E. Turkel, Preconditioned techniques in computational fluid dynamics,
738 *Annu. Rev. Fluid Mech.* 31 (1999) 385–416.
- 739 [12] J. S. W. D. L. Darmofal, J. Peraire, The solution of the compressible euler
740 equations at low mach numbers using a stabilized finite element algorithm,
741 *Comput. Methods Appl. Mech. Engrg.* 190 (2001) 5719–5737.
- 742 [13] X.-S. Li, C.-W. Gu, An all-speed roe-type scheme and its asymptotic anal-
743 ysis of low mach number behavior, *Journal of Computational Physics* 227
744 (2008) 5144–5159.
- 745 [14] J. L. Guermond, B. Popov, Viscous regularization of the euler equations
746 and entropy principles, under review.
- 747 [15] J. D. Anderson, Modern compressible flow, in: *Guide for Verification and*
748 *Validation in Computational Solid Mechanic.*, New York, 1982, pp. 10–
749 2006.

- [16] J. L. Guermond, R. Pasquetti, Entropy-based nonlinear viscosity for four-
 750 rier approximations of conservation laws, in: C.R. Math. Acad. Sci., Vol.
 751 326, Paris, 2008, pp. 801–806.
 752
- [17] V. Zingan, J. L. Guermond, J. Morel, B. Popov, Implementation of the
 753 entropy viscosity method with the discontinuous galerkin method, Journal
 754 of Comput. Phys 253 (2013) 479–490.
 755
- [18] E. F. Toro, Riemann Solvers and numerical methods for fluid dynamics,
 756 2nd Edition, Springer, 1999.
 757
- [19] B. Muller, Low-mach number asymptotes of the navier-stokes equations,
 758 Journal of Engineering Mathematics 34 (1998) 97–109.
 759
- [20] T. Alazard, A minicourse on the low mach number limit, Discrete and
 760 Continuous Dynamical Systems - Series S 1 (2008) 365–404.
 761
- [21] D. Gaston, C. Newsman, G. Hansen, D. Lebrun-Grandie, A parallel compu-
 762 tational framework for coupled systems of nonlinear equations, Nucl. Eng.
 763 Design 239 (2009) 1768–1778.
 764
- [22] R. Berry, R. Saurel, O. LeMetayer, The discrete equation method (dem)
 765 for fully compressible, two-phase flows in ducts of spatially varying cross-
 766 section, Nuclear Engineering and Design 240 (2010) 3797–3818.
 767
- [23] R. Loubere, Validation test case suite for compressible hydrodynamics com-
 768 putation, Theoretical Division T-7 Los Alamos National Laboratory.
 769
- [24] J. J. Quirk, A contribution to the great riemann solver debate, NASA
 770 Contractor Report 191409 ICASE Report No. (1992) 92–64.
 771
- [25] D. L. Darmofal, K. Siu, A robust multigrid algorithm for the euler equations
 772 with local preconditioning and semi-coarsening, Journal of Computational
 773 Physics 151 (1999) 728–756.
 774
- [26] P. Perrot, A to Z of Thermodynamics, Oxford University Press, 1998.
 775
- [27] S. LeMartelot, B. Nkonga, R. Saurel, Liquid and liquid-gas flows at all
 776 speeds., Journal of Computational Physics 255 (2013) 53–82.
 777
- [28] R. A. DeVore, G. G. Lorentz, Constructive Approximation, Springer-
 778 Verlag, 1991.
 779
- [29] R. Abgrall, R. Saurel, Discrete equations for physical and numerical
 780 compressible multiphase mixtures, Journal of Computational Physics 186
 781 (2003) 361–396.
 782
- [30] T. W. Roberts, The behavior of flux difference splitting schemes near slowly
 783 moving shock waves, Journal of Computational Physics 90 (1990) 141–160.
 784

785 **A. Derivation of the entropy residual as a function of density, pres-**
786 **sure and speed of sound**

The entropy residual is as follows:

$$R_e(\vec{r}, t) = \partial_t s(\vec{r}, t) + \vec{u} \cdot \vec{\nabla} s(\vec{r}, t),$$

where all variables were defined previously. This form of the entropy residual is not suitable for the low-Mach limit as explained in Section 2.1. In this appendix, we recast the entropy residual $R_e(\vec{r}, t)$ as a function of the primitive variables (pressure, velocity and density) and the speed of sound. The first step of this derivation is to use the chain rule, recalling that the entropy is a function of the internal energy e and the density ρ , yielding

$$R_e(\vec{r}, t) = s_e \frac{De}{Dt} + s_\rho \frac{D\rho}{Dt},$$

787 where s_e denotes the partial derivative of s with respect to the variable e . We
788 recall that $\frac{D}{Dt}$ denotes the material derivative. Since the internal energy e is a
789 function of pressure P and density ρ (through the equation of state), we use
790 again the chain rule to re-express the previous equation as a function of of the
791 material derivatives in P and ρ :

$$\begin{aligned} R_e(\vec{r}, t) &= s_e e_P \frac{DP}{Dt} + (s_e e_\rho + s_\rho) \frac{D\rho}{Dt} \\ &= s_e e_P \left(\frac{DP}{Dt} + \frac{1}{s_e e_P} (s_e e_\rho + s_\rho) \frac{D\rho}{Dt} \right) \\ &= s_e e_P \left(\frac{DP}{Dt} + \left(\frac{e_\rho}{e_P} + \frac{s_\rho}{s_e e_P} \right) \frac{D\rho}{Dt} \right). \end{aligned}$$

We are now close to the final result (see Eq. (9)). To prove that the term multiplying the material derivative of the density is indeed equal to the square of the speed of sound, we recall that the speed of sound is defined as the partial derivative of pressure with respect to density at constant entropy, which can be recast as a function of the entropy as follows (see Appendix A.2 of [14]):

$$c^2 := \left. \frac{\partial P}{\partial \rho} \right|_{s=cst} = P_\rho - \frac{s_\rho}{s_e} P_e.$$

Using the following relations (see Appendix A.1 of [14])

$$P_e = \frac{1}{e_P} \text{ and } P_\rho = -\frac{e_\rho}{e_P},$$

Eq. (9) is obtained and recalled below for completeness:

$$R_e(\vec{r}, t) := \partial_t s + \vec{u} \cdot \vec{\nabla} s = \frac{Ds}{Dt} = \frac{s_e}{P_e} \left(\underbrace{\frac{DP}{Dt} - c^2 \frac{D\rho}{Dt}}_{\widetilde{R}_e(\vec{r}, t)} \right).$$

792 **B. Derivation of the dissipative terms for the Euler equations with**
 793 **variable area using the entropy minimum principle**

794 Euler equations (without viscous regularization) with variable area are re-
 795 called here

$$\partial_t (\rho A) + \vec{\nabla} \cdot (\rho \vec{u} A) = 0 \quad (42a)$$

$$\partial_t (\rho \vec{u} A) + \vec{\nabla} \cdot [A (\rho \vec{u} \otimes \vec{u} + P \mathbf{I})] = P \vec{\nabla} A \quad (42b)$$

$$\partial_t (\rho E A) + \vec{\nabla} \cdot [\vec{u} A (\rho E + P)] = 0. \quad (42c)$$

798 The specific entropy is a function of the density ρ and the internal energy e , i.e.,
 799 $s(e, \rho)$, the above system of equations satisfies the minimum entropy principle
 800 [18] *is this really shown in Toro? I think it is and will double check tomorrow*

$$A \rho \left(\partial_t s + \vec{u} \cdot \vec{\nabla} s \right) \geq 0. \quad (43)$$

801 The entropy function s satisfies the second law of thermodynamics, $T ds =$
 802 $de - \frac{P}{\rho^2} d\rho$, which implies $s_e := T^{-1}$ and $s_\rho := -PT^{-1}\rho^{-2}$. One can show that
 803 [14]

$$s_e = T^{-1} \geq 0 \text{ and } P s_e + \rho^2 s_\rho \quad (44)$$

804 In order to apply the entropy viscosity method to the variable-area Euler equa-
 805 tions, dissipative terms need to be added to each equation in Eq. (42). The
 806 functional forms of these terms need to be such that the entropy residual de-
 807 rived with these terms present also satisfies the minimum entropy principle. To
 808 prove the minimum entropy principle, the extra terms appearing in the entropy
 809 residual are either recast as conservative terms or shown to be positive. The
 810 rest of this appendix presents this demonstration. Following [14], we first write
 811 the variable-area equation with dissipative terms.

$$\partial_t (\rho A) + \vec{\nabla} \cdot (\rho \vec{u} A) = \vec{\nabla} \cdot f \quad (45a)$$

$$\partial_t (\rho \vec{u} A) + \vec{\nabla} \cdot [A (\rho \vec{u} \otimes \vec{u} + P \mathbf{I})] = P \vec{\nabla} A + \vec{\nabla} \cdot g \quad (45b)$$

$$\partial_t (\rho E A) + \vec{\nabla} \cdot [\vec{u} A (\rho E + P)] = \vec{\nabla} \cdot (h + \vec{u} \cdot g). \quad (45c)$$

where f , g and h are dissipative fluxes to be determined. Starting from the
 modified system of equations given in Eq. (45), the entropy residual is derived
 again. The derivation requires the following steps : express the governing laws
 in terms of primitive variables (ρ, \vec{u}, e) , multiply the continuity equation by ρs_ρ
 and the internal energy equation by s_e , and invoke multivariate chain rule, e.g.,
 $\partial s / \partial x = s_e \partial e / \partial x + s_\rho \partial \rho / \partial x$. These steps are similar to the ones from the
 standard Euler equations [14]. Some of the lengthy algebra is omitted here.
 The above steps yield:

$$A \rho \left(\partial_t s + \vec{u} \cdot \vec{\nabla} s \right) = s_e \left[\vec{\nabla} \cdot h + g : \vec{\nabla} u + \left(\frac{u^2}{2} - e \right) \vec{\nabla} \cdot f \right] + \rho s_\rho \vec{\nabla} \cdot f \quad (46)$$

814 The next step consists of choosing a definition for each of the dissipative terms
 815 so that the left hand-side is positive. The right hand-side of Eq. (46) can be
 816 simplified using the following relations, $g = A\mu\vec{\nabla}^s\vec{u} + f\otimes\vec{u}$ and $h = \tilde{h} - 0.5\|\vec{u}\|^2 f$,
 817 which yields:

$$A\rho\left(\partial_t s + \vec{u} \cdot \vec{\nabla} \cdot s\right) = s_e \left[\vec{\nabla} \cdot \tilde{h} - e\vec{\nabla} \cdot f \right] + \rho s_\rho \vec{\nabla} \cdot f + A s_e \mu \vec{\nabla}^s \vec{u} : \vec{\nabla} \vec{u}$$

818 The right hand-side is now integrated by parts:

$$\begin{aligned} A\rho\left(\partial_t s + \vec{u} \cdot \vec{\nabla} \cdot s\right) &= \vec{\nabla} \cdot \left[s_e \tilde{h} - s_e e f + \rho s_\rho f \right] - \\ &\quad \vec{\nabla} \cdot \tilde{h} \vec{\nabla} s_e + f \cdot \vec{\nabla} (e s_e) - f \cdot \vec{\nabla} (\rho s_\rho) + A s_e \mu \vec{\nabla}^s \vec{u} : \vec{\nabla} \vec{u} \end{aligned}$$

819 where $\vec{\nabla}^s$ is the symmetric gradient. The term $A s_e \mu \vec{\nabla}^s \vec{u} : \vec{\nabla} \vec{u}$ is positive and
 820 thus, does not need any further modification. It remains to treat the other
 821 terms of the right hand-side that we now call rhs :

$$rhs = \vec{\nabla} \cdot \left[s_e \tilde{h} - s_e e f + \rho s_\rho f \right] - \tilde{h} \cdot \vec{\nabla} s_e + f \cdot \vec{\nabla} (e s_e) - f \cdot \vec{\nabla} (\rho s_\rho)$$

822 The first term of rhs is a conservative term. By choosing carefully a definition
 823 for \tilde{h} and f , the conservative term can be expressed as a function of the entropy
 824 s . It is also required to include the variable area in the choice of the dissipative
 825 terms so that when assuming constant area, the regular multi-D Euler equations
 826 are recovered. The following definitions for \tilde{h} and f are chosen:

$$\tilde{h} = A\kappa\vec{\nabla}(\rho e) \text{ and } f = A\kappa\vec{\nabla}\rho,$$

827 which yields, using the chain rule:

$$rhs = \vec{\nabla} \cdot (\rho A\kappa\vec{\nabla}s) - A\kappa \underbrace{\left[\vec{\nabla}(\rho e)\vec{\nabla}s_e - \vec{\nabla}\rho\vec{\nabla}(e s_e) + \vec{\nabla}\rho\vec{\nabla}(\rho s_\rho) \right]}_{\mathbf{Q}}$$

828 It remains to treat the term \mathbf{Q} that can be recast under a quadratic form,
 829 following the work done in [14]:

$$\begin{aligned} \mathbf{Q} &= X^t \Sigma X \\ \text{with } X &= \begin{bmatrix} \vec{\nabla}\rho \\ \vec{\nabla}e \end{bmatrix} \text{ and } \Sigma = \begin{bmatrix} \partial_\rho(\rho^2\partial_\rho s) & \partial_{\rho,e}s \\ \partial_{\rho,e}s & \partial_{e,e}s \end{bmatrix} \end{aligned}$$

830 The matrix Σ is symmetric and identical to the matrix obtained in [14]. The sign
 831 of the quadratic form can be simply determined by studying the positiveness of
 832 the matrix Σ . In this particular case, it is required to prove that the matrix is
 833 negative definite: the quadratic form is in the right hand-side and is preceded of
 834 a negative sign. According to [14], the convexity of the opposite of the entropy
 835 function s with respect to the internal energy e and the specific volume $1/\rho$ is
 836 sufficient to ensure that the matrix Σ is negative definite.

837 Thus, the right hand-side of the entropy residual Eq. (46), are now either recast
 838 as conservative terms, or known to be positive. Following the work done by [14],
 839 the entropy minimum principle holds.

840 **C. Entropy residual with an isentropic equations of state:**

841 This appendix aims at showing that the entropy residual is null when as-
 842 suming an isentropic flow.

843 The entropy residual as a function of the pressure, the density, the velocity and
 844 the speed of sound is recalled here:

$$\widetilde{R}_e = \frac{dP}{dt} - c^2 \frac{d\rho}{dt} \quad (47)$$

845 Assuming an isentropic flow, the pressure is only a function of the density as
 846 follows: $P = f(\rho)$ or $\rho = f^{-1}(P)$. Using the definition of the speed of sound
 847 $c^2 = \left. \frac{\partial P}{\partial \rho} \right)_s$ and the above form the equation of state, the following relation is
 848 derived:

$$c^2 = \left. \frac{\partial P}{\partial \rho} \right)_s = \frac{dP}{d\rho} = \frac{df(\rho)}{d\rho} \quad (48)$$

849 Using the chain rule, the entropy residual of Eq. (47) can be recast as a function
 850 of the density, the velocity and the speed of sound, and proven equal to zero:

$$\begin{aligned} \widetilde{R}_e &= \frac{df(\rho)}{d\rho} \frac{d\rho}{dt} - c^2 \frac{d\rho}{dt} \\ \widetilde{R}_e &= c^2 \frac{d\rho}{dt} - c^2 \frac{d\rho}{dt} \\ \widetilde{R}_e &= 0 \end{aligned}$$